



Co-funded by the Erasmus+ Programme of the European Union





REMOTE SENSING IN AGRICULTURAL WATER MANAGEMENT

2020-1-TR01-KA202-094374

IMPROVING AGRICULTURAL WATER USE EFFICIENCY BY USING SATELLITE AND UN-MANNED AIR VEHICLE SYSTEMS

Edited by: Dr. Sakine Çetin Taner Dr. Eyüp Selim Köksal

Technical Report -I

2023

Co-funded by the
Erasmus+ Programme
of the European Union

Table of Contents

1. INTRODUCTION

Dr. Sakine Çetin Taner

Agriculture provides humanity with critical raw materials such as food, fiber and fuel, which are crucial for human subsistence. Today, this role needs to be fulfilled in the context of environmental sustainability and climate change. With the increasing human population, agricultural activities must maintain their continuity to ensure human livelihoods (Weiss et al., 2020). The transition from intensive to sustainable agriculture should consider unexpected climatic conditions or extreme climatic events (e.g., changes in temperature and rainfall) (Tirado et al., 2010; Weiss et al., 2020).

Agriculture is the primary sectoral user of freshwater worldwide and a significant source of environmental degradation (Zhang et al., 2019; Foster et al., 2020; Tang et al., 2020). As competition over limited land and water resources increases, policy makers in many regions seek to limit agricultural water withdrawals, improve irrigation water use efficiency, and develop new effective resource utilization strategies (Foster et al., 2020; Tang et al., 2020). The policies and interventions proposed or implemented by countries, pumping quotas, energy costs, taxes, water pricing, and many other factors vary between regions (Palazzo and Brozović, 2014; Fishman et al., 2016; Aarnoudse et al., 2019; Rad et al., 2020; Rouillard, 2020; Sidhu et al., 2020). Despite the importance of monitoring for water management worldwide, most agricultural water use (from both groundwater and surface water) is not measured (Scanlon et al., 2012; Grafton, 2019; Hanemann and Young, 2020).

Due to the technical, economic, and practical difficulties associated with on-site measurement, there is a need for water managers and researchers to monitor agricultural water use and plant growth and condition at different spatial and temporal scales for other purposes (Foster et al., 2020; Weiss et al., 2020). Real-time monitoring is essential to minimise the impacts of changing climatic conditions on the global food system and optimise agricultural water management practices sustainably (Wheeler and von Braun, 2013; Areal et al., 2018). Remote sensing is essential to respond to all these requirements locally and globally. The basic principle in remote sensing is using the electromagnetic spectrum (visible, infrared, and microwaves) to evaluate some features on Earth. The response of objects to different

wavelength regions varies, so they are used to distinguish vegetation, bare soil, water, and other similar features (Shanmugapriya et al., 2019).

Monitoring agriculture through remote sensing is widely addressed with specific applications such as agricultural meteorology, precision agriculture, yield estimation, plant growth and development monitoring, vegetation mapping, disease and pest tracking, irrigation monitoring, and weed detection. Specific remote sensing platforms (e.g., satellites, Unmanned Aerial Vehicles (UAV), Unmanned Ground Vehicles (UGV), etc.) or sensors (e.g., active or passive sensing, wavelength domain, spatial sampling) are used in different locations and climates (e.g. country or continent, wetlands or drylands etc.) (Ambika et al., 2016; Deines et al., 2019; Vogels et al., 2019; Shanmugapriya et al., 2019; Weiss et al., 2020).

This study aims to prepare a technical report on remote sensing techniques used in agricultural water management within the scope of this Erasmus+ project. For this purpose, in this study, the methods available in the literature from the past to the present and frequently used techniques have been compiled and brought together.

References

Aarnoudse, E., Bluemling, B., Qu, W., and Herzfeld, T. (2019). Groundwater regulation in case of overdraft: National groundwater policy implementation in north-west China.International Journal of Water Resources Development,35(2), 264–282.

Ambika, A. K., Wardlow, B., and Mishra, V. (2016). Remotely sensed high resolution irrigated area mapping in India for 2000 to 2015. Scientific Data,3(1), 1–14.

Areal, F. J., Jones, P. J., Mortimer, S. R., and Wilson, P. (2018). Measuring sustainable intensification: Combining composite indicators and efficiency analysis to account for positive externalities in cereal production. Land Use Policy, 75, 314-326.

Deines, J. M., Kendall, A. D., Butler, J. J., and Hyndman, D. W. (2019). Quantifying irrigation adaptation strategies in response to stakeholder-driven groundwater management in the US High Plains Aquifer.Environmental Research Letters,14, 44014.

Fishman, R., Lall, U., Modi, V., and Parekh, N. (2016). Can electricity pricing save India's groundwater? Field evidence from a novel policy mechanism in gujarat.Journal of the Association of Environmental and Resource Economists,3(4), 819–855.

Foster, T., Mieno, T., and Brozović, N. (2020). Satellite-based monitoring of irrigation water use: Assessing measurement errors and their implications for agricultural water management policy. *Water Resources Research*, *56*(11), e2020WR028378.

Grafton, R. Q. (2019). Policy review of water reform in the Murray–Darling Basin, Australia: The "do's" and "do'nots".Australian Journal of Agricultural and Resource Economics,63(1), 116–141.

Hanemann, M., and Young, M. (2020). Water rights reform and water marketing: Australia vs the US West.Oxford Review of Economic Policy,36(1), 108–131.

Palazzo, A., and Brozovi´c, N. (2014). The role of groundwater trading in spatial water management.Agricultural Water Management,145,50–60.

Rad, M. R., Brozovi´c, N., Foster, T., and Mieno, T. (2020). Effects of instantaneous groundwater availability on irrigated agriculture and implications for aquifer management. Resource and Energy Economics,59, 101129.

Rouillard, J. (2020). Tracing the impact of agricultural policies on irrigation water demand and groundwater extraction in France, Sustainable groundwater management (pp. 461–479). London, UK: Springer.

Scanlon, B. R., Faunt, C. C., Longuevergne, L., Reedy, R. C., Alley, W. M., McGuire, V. L., and McMahon, P. B. (2012). Ground water depletion and sustainability of irrigation in the US High Plains and Central Valley. Proceedings of the National Academy of Sciences,109(24), 9320–9325.

Shanmugapriya, P., Rathika, S., Ramesh, T., and Janaki, P. (2019). Applications of remote sensing in agriculture-A Review. Int. J. Curr. Microbiol. Appl. Sci, 8(01), 2270-2283.

Sidhu, B. S., Kandlikar, M., and Ramankutty, N. (2020). Power tariffs for groundwater irrigation in India: A comparative analysis of the environmental, equity, and economic tradeoffs.World Development,128, 104836.

Tang, Y., Zhang, F., Engel, B. A., Liu, X., Yue, Q., and Guo, P. (2020). Grid-scale agricultural land and water management: A remote-sensing-based multiobjective approach. *Journal of Cleaner Production*, *265*, 121792.

Tirado, M. C., Clarke, R., Jaykus, L. A., McQuatters-Gollop, A., and Frank, J. M. (2010). Climate change and food safety: A review. *Food Research International*, *43*(7), 1745-1765.

Vogels, M. F. A., De Jong, S. M., Sterk, G., Douma, H., and Addink, E. A. (2019). Spatio-temporal patterns of smallholder irrigated agriculture in the horn of Africa using GEOBIA and Sentinel-2 imagery.Remote Sensing,11(2), 143.

Weiss, M., Jacob, F., and Duveiller, G. (2020). Remote sensing for agricultural applications: A meta-review. *Remote sensing of environment*, *236*, 111402.

Wheeler, T., and Von Braun, J. (2013). Climate change impacts on global food security. Science, 341(6145), 508-513.

Zhang, F., Yue, Q., Engel, B. A., Guo, S., Guo, P., and Li, X. (2019). A bi-level multiobjective stochastic approach for supporting environment-friendly agricultural planting strategy formulation. *Science of The Total Environment*, *693*, 133593.

2. PRINCIPLES OF REMOTE SENSING

Jitka Kumhálová *František Kumhála*

Remote Sensing (RS) is a method of obtaining information about objects and phenomena on the surface of the planet Earth without the need for physical contact. The English term "Remote Sensing" was introduced in the mid-1950s by geographer and oceanographer Evelyn Pruitt from the U.S. Office of Naval Research as a reaction to the fact that the term "aerial photography" used until then no longer covered the actual state of the technologies used (Herring, 2005).

Each Remote Sensing system consists of four essential components:

- Observed scene (landscape, water objects, and others), including the surrounding environment (e.g., atmosphere) and their corresponding characteristics.
- Energy sources (Electro-magnetic radiation : EMR) (Purcell and Morin, 2013).
- Measuring equipment is placed on a suitable carrier (aircraft, satellite, drone, etc.). The apparatus usually consists of detectors of various types, such as cameras, radiometers, lasers, radio frequency receivers, radar systems, sonars, seismographs, gravimeters, and others).
- A processing system consists of two processing stages – data pre-processing on board the carrier and data processing using a particular SW, including data processing using GIS tools.

2.1. Data acquisition system

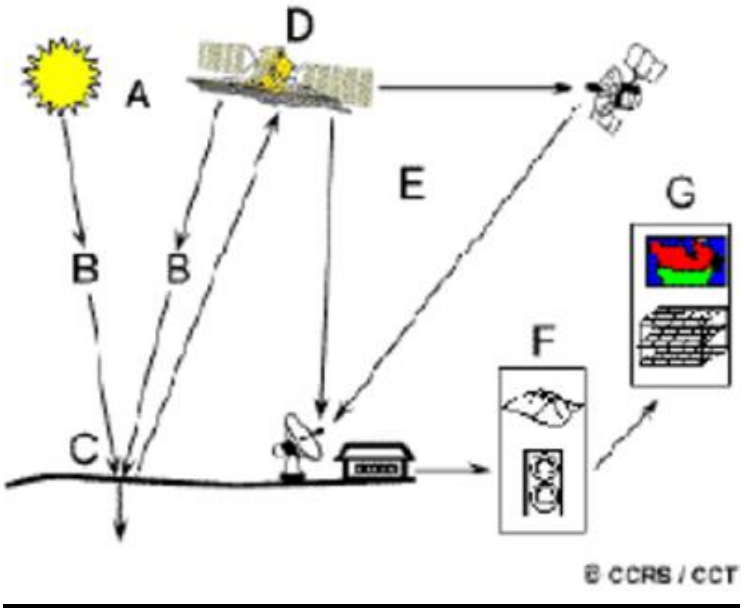

Figure 2.1 Data acquisition system (Anonymous, 2023a)

Where (Figure 2.1):

A : Source of Radiation: The first requirement of RS is to have a radiation source that interacts with the object under investigation.

B : Radiation and the Atmosphere: As the radiation goes from the source to the target object and from the target object to the satellite, it passes through the atmosphere - where the radiation interacts and is modified.

C : Interaction with target object: Once the radiation penetrates the atmosphere, it interacts with the object of interest. It depends here on the properties of the object, as well as on the properties of the radiation.

D : Record of reflected radiation by the sensor: A recording occurs on the sensor after the radiation is reflected (or even the object itself can radiate).

E : Transmission and Processing: The record is transferred, mostly in electronic form, to a receiving station, where the data is processed into an image; it often goes through pre-processing and corrections.

F : Interpretation and Analysis: Image processing and interpretation (visual, digital), information extraction, GIS.

G . Application: the last step of RS is obtaining information about the target object solving the problem – GIS application.

Each image, like a map, contains two types of information:

- About the type of object or phenomenon – thematic map
- About the location of objects – topographic map

Information about the type of objects or phenomena in the images is obtained through the process of interpretation and classification of the images.

An essential part of RS is "Photogrammetry," which deals with processing information about the correct position of objects in the images. It is a technical discipline that deals with the measurement properties of images to create accurate topographic maps. It was initially involved in the processing of aerial photographs. In recent decades, it has also been processing satellite images and images from unmanned aerial vehicles (UAV).

Distribution of Remote Sensing of Earth methods:

According to the image recording method:

Classical - conventional

- The result is a photograph in analog ("paper") form.
- A photograph is created in a "moment."
- Quality mostly depends on weather conditions.
- It is geometrically accurate.
- It has certain limitations regarding the analysis of thematic information.
- The photographs cover a much larger time interval (half of the 20th century).

Unconventional

- Images are created gradually by scanning individual lines - the so-called line scanning.
- Recording using radiometers – measures radiation.
- Scanners – scanning decomposition devices
- Smaller spatial resolution
- Data on the wider part of EM spectra
- Data in digital form

According to the source, Electro Magnetic (EM) radiation:

*Passive methods (*Figure 2.2*)*

- direct - the source of the Sun, the output is every photo.
- Indirect – objects on Earth are the source of thermal imaging.

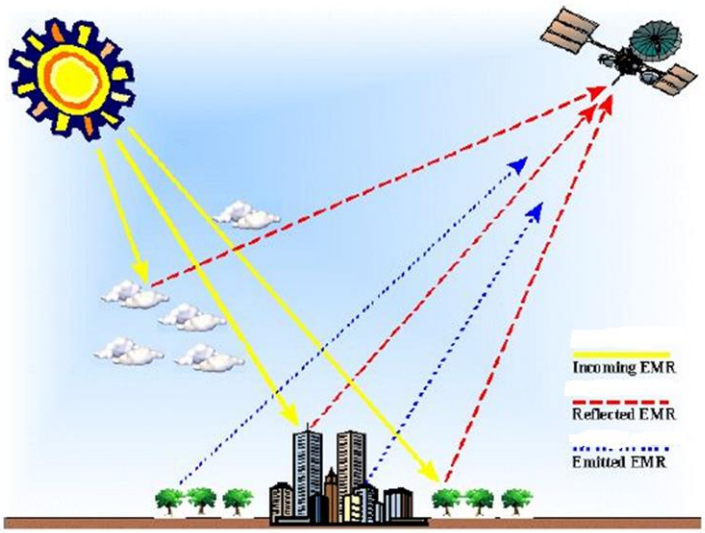

Figure 2.2 Passive EM radiation (Dobrovolný, 1998).

Active methods

- the source is not of natural origin.
- Is transmitted by a carrier.
- E.g., radar systems.

According to the type of carrier:

- planes
- satellites
- UAVs
- balloons
- models

According to the recordable part of the spectrum:

- panchromatic – B&W
- multispectral

- infrared
- thermal
- radar

By colours:

- B&W
- colored – in false colors or natural colors

2.2. Physical principles of Remote Sensing

Substances of all states emit Electro Magnetic Radiation (EMR), the origin of which is related to the disordered movement of electrically charged particles in the electron shells of their atoms. We refer to such radiation as thermal radiation (Figure 2.3).

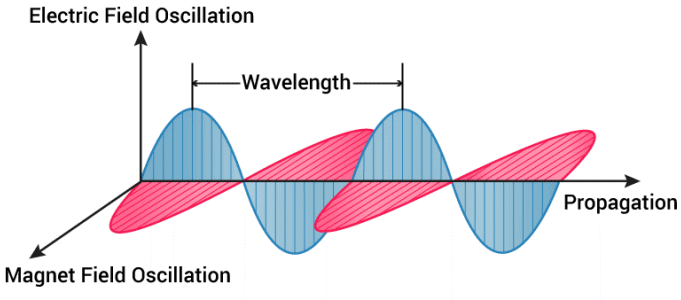

Figure 2.3 Principles of EMR (Anonymous 2023b).

All physical entities with an internal temperature above 0 K can be a source of energy in the form of thermal electromagnetic radiation.

EMR is the vector as well as the object of the photon or energy flow. The energy is transported by the propagation of disturbances in electric (E) and magnetic fields (B):

- EMR waves propagate at the speed of light *c*, where *c* = 300 000 *km/second*
- Wavelength λ can be defined graphically as the interval or spacing between the wave crests.
- Frequency (marked ν or μ) represents the number of wave crests that pass a particular point in space in one second.
- EMR waves that have a constant frequency are called monochromatic.

- Wavelength is universally expressed in metric units such as μm or nm.
- Frequency is expressed in Hertz.
- The longer λ is, the lower the energy content or ν must be.
- When EMR passes from one medium into another, λ and c change while ν is source-specific and remains constant.

EMR wave properties can be grouped in two categories:

- Permanent characteristics (such as wavelength and frequency) - constant for a given observation system.
- Variable characteristics (such as amplitude, phase, polarization and propagation direction) – the interaction between matter and energy may impact it.

The energy **E** carried by a single photon of EMR with a specific frequency **ν** is given by:

$$\mathbf{E = h\,\nu}$$

$$\boldsymbol{E} = (\boldsymbol{h}\,\boldsymbol{c})/\boldsymbol{\lambda}$$, where h = Planck`s constant

The emission of EMR is, first and foremost, a product of thermal radiation, and the wavelength of the emittance is a function of the body's absolute temperature.
In addition to emitting radiation, each body can reflect, transmit, and absorb radiation. The absorbed radiation is mainly converted into thermal energy. The amount of absorbed radiation depends on the properties of the body, especially the color (black bodies absorb more radiation than white) and the surface finish (radiation is reflected from shiny bodies, while dull bodies absorb more radiation).

A physical abstraction is introduced for an easier and more accurate description of radiation sources - an absolutely black body (e.g. Planck, 1914). Its name corresponds to the fact that the black body perfectly absorbs all the energy that falls on the body. There is no radiation reflection, so this body appears perfectly black to us at low temperatures.
A relatively good model of an absolute black body is a cavity, the inner surface of which is a matte black surface. If electromagnetic radiation penetrates through the opening, all the energy of the radiation is absorbed during repeated reflections from the walls of the cavity. The opening of the cavity then appears as a black body (Figure 2.4).

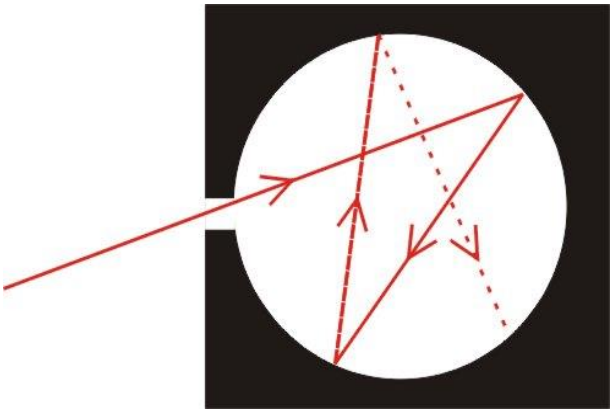

Figure 2.4 Model of "an absolute black body" (*Dobrovolný, 1998)*.

The first mentions of so-called thermal radiation appeared in the second half of the 18th century - Karl Scheele (1742-86).

The first experiments were carried out by Marcus Pictet (1752-1825).
Based on them, Pierre Prévost (1751-1839) assumed that each body radiates independently of its surroundings.

Another shift was brought by the works of the German physicist Gustav Kirchhoff (Figure 2.5), who proved the relationship between the emission and absorption of radiation, founded the spectral analysis of substances, and defined the concept of an absolute black body.

Figure 2.5 Gustav Kirchhoff (Von Laue, 1958).

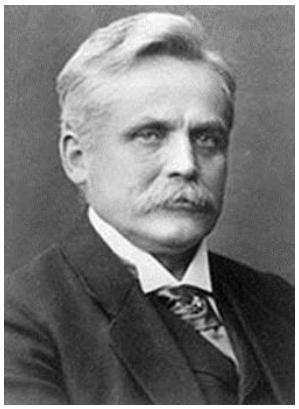

Figure 2.6 Wilhelm Wien (Von Laue, 1958).

Basic physical laws:

- **Wien's displacement law:** As the temperature increases, the peak exitance migrates toward the shorter wavelengths (e.g., A dictionary of Physics, 2009). Wilhelm Wied – Figure 2.6, Wien's displacement law – Figure 2.7).

$\boldsymbol{\lambda max}$= $\boldsymbol{b/T}$, where b = constant = 2898 μm.K;

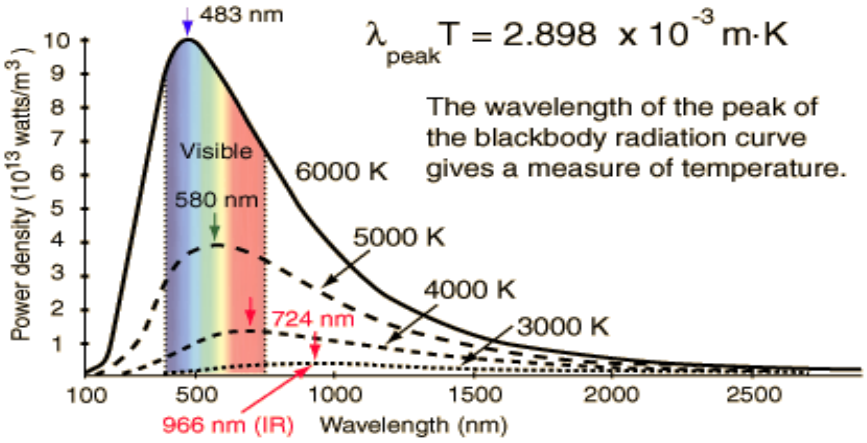

Figure 2.7 Wien's displacement law (Anonymous, 2023c).

Austrian physicists Josef Stefan and Ludwig Boltzmann also tried to describe blackbody radiation using classical physics, who derived the dependence of the intensity of blackbody radiation on its thermodynamic temperature.

- **Stefan Boltzmann's law:** The higher the temperature, the greater the spectral exitance.

$\boldsymbol{E}$= $\boldsymbol{\varepsilon\sigma T4/\lambda}$, where E = radiant exitance; $\boldsymbol{\sigma}$ = Stefan Boltzmann constant; $\boldsymbol{\varepsilon}$ = emissivity factor; T = temperature in degrees Kelvin

Each body with a non-zero absolute temperature radiates, with the radiation intensity (radiant flux density) being proportional to the fourth power of the absolute temperature (e.g., Siegel and Howell, 1992).

However, they arrived at only approximate results, just like the Englishmen John Strutt (Lord Rayleigh) and Sir James Jeans, who derived the law describing the radiation of a black body. Unfortunately, it was only valid in the long-wave range of the spectrum.

Only the German physicist Max Planck (Figure 2.8) removed all the shortcomings of the laws describing black body radiation. After graduation, despite the advice of his physics professor, he focused on physics, specifically classical thermodynamics and the description of blackbody

radiation. In deriving the properties of a black body, he introduced the simplifying assumption that a black body cannot emit or absorb energy in arbitrarily large quantities but only in specific "packages" - quanta. He assigned energy to each quantum of radiation that is directly proportional to the frequency of the radiation according to the following equation:

Figure 2.8 Max Planck (Von Laue, 1958)

$$E = hf = \frac{hc}{\lambda},$$

Where E is the energy of a quantum of radiation; h is Planck's constant (h = 6.626.10-34 J.s); f is frequency; c is the speed of light in a vacuum.

Max Planck defined the theory: EM radiation consists of individual particles – photons, quanta.

Summary

- The longer the wavelength, the lower the energy content of the radiation.
- Naturally, emitted long-wave radiation will be harder to detect than short-wave energy.
- The low energy content of long-wave radiation means that systems operating in long wavelengths must scan large areas of the earth's surface in one measurement to receive a signal that the measuring apparatus can record.
- The higher the body's temperature, the more it will emit energy with a shorter wavelength.
- "Hot" objects will intensely emit high-frequency, short-wave radiation. They will, therefore, be easily detectable by RS methods.
- Conversely, "cold" objects will emit less intense long-wave radiation. They will be harder to detect.

- However, the atmosphere transmits long-wave radiation well and absorbs and scatters short waves.

- **Kirchhoff's law**

Objects of the same temperature can emit different amounts of energy, but always less than an absolute black body (e.g., Goody and Yung, 1989).

The so-called emissivity (ε) is the ratio between the intensity of radiation of a real body (M_R) and the intensity of radiation of a black body (M_A) at a given temperature T:

$$\varepsilon = \frac{M_R}{M_A}$$

Emissivity is essential for determining the temperature characteristics of surfaces.

Influence of electromagnetic radiation by the atmosphere

The effects of the atmosphere on radiation characteristics depend on the following factors:

- The length of the path that this radiation takes through the atmosphere.
- Sizes of the emitted signal.
- Atmospheric conditions.
- Wavelength.

Radiation is mainly influenced by absorption and scattering processes:

- Dispersion causes higher values of measured radiation, especially in shorter wavelengths.
- The measured values of electromagnetic radiation in longer wavelengths are then reduced by absorption.

Scattering of radiation

- *Rayleigh scattering* occurs on gas molecules or other particles significantly smaller than the wavelength – dust particles, oxygen, and nitrogen molecules; shorter wavelengths are scattered more than longer wavelengths. It is the dominant phenomenon at the upper boundary of the atmosphere; it causes the blue color of the sky.
- *Mie scattering* occurs when the particles are approximately the same size as the wavelength of the radiation – dust, pollen grains, smoke, water vapor. It affects longer wavelengths. It is dominant in the lower layers of the atmosphere.

- *Non-selective scattering* – it does not depend on the wavelength. It, therefore, causes an equally intense scattering of all wavelengths in the visible part of the spectrum, and the result is, for example, the white color of clouds and fog (Figure 2.9).

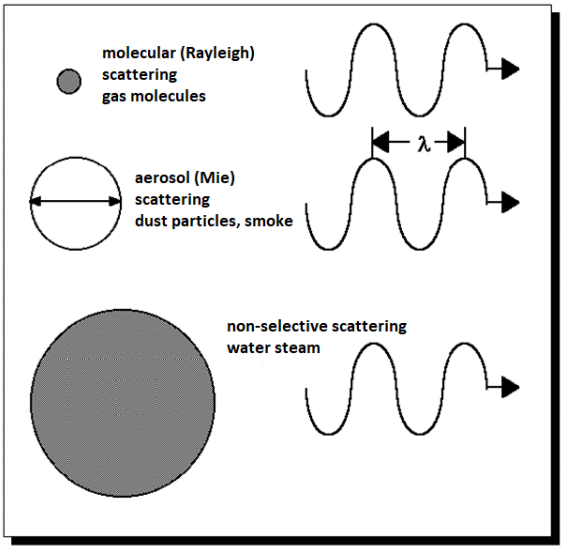

Figure 2.9 The types of scattering (Dobrovolný, 1998).

The scattering of radiation in the atmosphere is primarily a function of wavelength. The intensity of molecular scattering is inversely proportional to the fourth power of the wavelength, where blue light (0.4 μm) is scattered 16 times more than infrared radiation with a wavelength of 0.8 μm.

Absorption of radiation

It is the cause of energy losses at a given wavelength. The main gases absorbing radiation are O_3, CO_2, and water vapor. The mentioned gases absorb radiation with varying intensity in certain wavelength intervals, making it practically impossible to record and measure the intensity of EM radiation. Parts of the EM spectrum unaffected by absorption and scattering are called atmospheric windows (Table 2.1).

Table 2.1 The main atmospheric windows.

Part of EM spectrum	Interval of wavelength (µm)
UV /visible	0.30 – 0.75
	0.77 – 0.91
Near-infrared	1.00 – 1.12
	1.19 – 1.34
	1.55 – 1.75
	2.05 – 2.40
Middle infrared	3.50 – 4.16
	4.50 – 4.00
Thermal infrared	8.00 – 9.20
	10.20 – 12.40
	17.00 – 22.00

Impact of radiation on the earth's surface

- EM energy can be reflected or absorbed.
- Two objects that reflect similar amounts of radiation in one wavelength interval may reflect different amounts of energy in another interval.
- The amount of absorbed or reflected energy affects the physical and chemical properties of surfaces (temperature, water or organic matter content, surface roughness, etc.).
- Static and dynamic parameters.
- The reflective properties of surfaces, depending on the wavelength and the physical and chemical properties of the surfaces, shape their so-called spectral behavior.

2.3. Basic areas of the spectrum usable in Remote Sensing

Because of the atmosphere (absorption and scattering radiation), images can only be created in certain parts of the spectrum (Figure 2.10) (e.g. Browne, 2013):

- Ultraviolet radiation – ultraviolet (UV): 0.1 – 0.4 µm
- Visible radiation – visible (VIS): 0.4-0.7 µm
- Near infrared radiation – near infrared (NIR or IR): 0.7 – 1.4 µm
- Middle infrared radiation (MIR): 1.4 – 3 µm

- Thermal radiation – thermal infrared – thermal (TIR or IR): 3 µm – 1 mm
- Microwave radiation – microwave: 1 mm – 1 mm

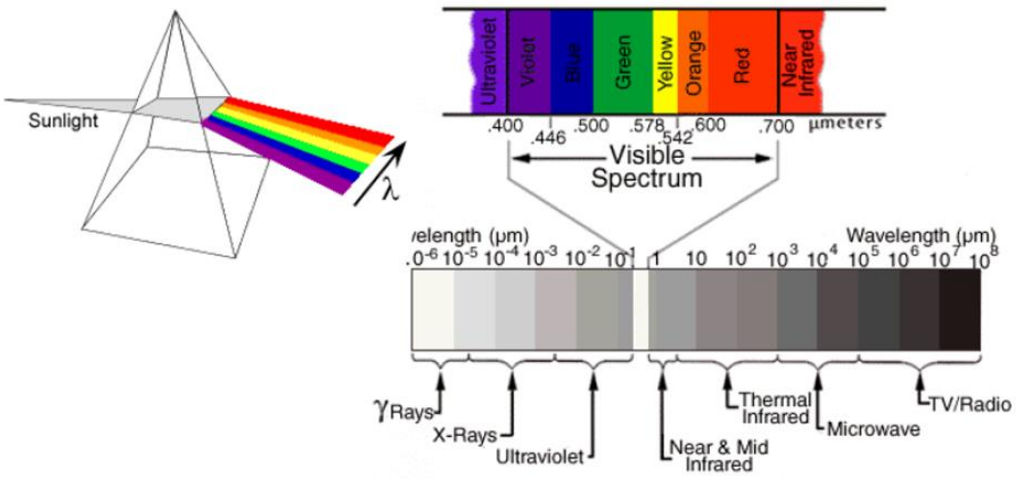

Figure 2.10 Electromagnetic spectrum (Dobrovolný, 1998).

Ultraviolet rays

- It is radiation harmful to living organisms.
- Only a small part is released to the earth's surface.
- In RS, it is used in the form of a so-called UV laser.
- It can be used to search for gold deposits and monitor oil spills.
- This radiation also passes through the water column to some extent.
- Many minerals emit characteristic radiation at these wavelengths (used in mineralogy).
- The intensity of absorption of UV radiation by O_3 is used to monitor the strength of the ozone layer.

Visible radiation

- In the field of visible radiation, all conventional methods work, as well as most satellite systems.
- It is the most used part of the spectrum, especially from a historical point of view.
- It does not pass through clouds and fog; it can only be recorded during daylight hours.
- Considerable scattering and absorption result in, for example, a loss of contrast in visible images.

- Compared to other wavelengths, this radiation can pass through the water column – especially in the blue part of the spectrum.
- This makes it possible to study many physical and biological properties of water bodies.
- Individual rocks, minerals, or soil do not show differences in spectral behavior in the visible part of the spectrum.

Near-infrared (NIR – near infrared)

- It forms a continuation of the atmospheric window from the visible part of the spectrum.
- It can be recorded electronically by conventional photographic methods (up to 0.9 μm).
- It is already less absorbed and scattered by the atmosphere.
- As a result, images are sharp with good contrast.
- Suitable for topographical purposes, these wavelengths are essential for studying vegetation, especially in forestry and agriculture.
- Water behaves almost like an absolute black body at these wavelengths.

Mid-infrared

- It includes two atmospheric windows with centers of approximately 1.5 and 2.2 μm.
- Both are important primarily for vegetation and geological studies.
- The first window, for example, enables a good differentiation of vegetation types. It is suitable for recognizing ice and snow, distinguishing cloudiness, and studying vegetation's health status.
- The second window is the region where many minerals have a characteristic absorption band.
- The amount of reflected radiation is significantly greater than that of emitted radiation. Due to this small amount of radiation emitted, near and mid-infrared wavelengths cannot be used to determine the thermal properties of surfaces.
- This is only possible in thermal infrared radiation, where the proportion of emitted radiation is more significant.

Thermal Infrared Radiation (TIR)

- It contains two atmospheric windows at 3–5 and 8–14 μm intervals.

- The images are used, for example, to determine the sea surface temperature, to map the thermal pollution of rivers and lakes and the landscape itself, to locate forest fires, etc.
- Since the amount of reflected radiation is still relatively large in the 3-5 μm region, only night hours can be used to measure the radiation temperature.
- In the area of 8-14 μm, the amount of reflected solar radiation is already minimal compared to the emitted radiation; these wavelengths can then be used to determine the radiation temperature even during daylight hours.
- Accurate quantitative measurements require a good knowledge of the so-called emissivity of objects and processes that affect radiation in the atmosphere.
- In the case of accurate calibration, the images allow us to obtain knowledge about the thermal balance of objects.

Microwave radiation

- It is used by both passive and active methods (RADAR).
- These long wavelengths can also penetrate below the surface under suitable conditions.
- It is the least envious of weather conditions; it is significantly weakened only in case of heavy rain.
- The intensity of naturally emitted microwave radiation is very low, so the measuring device must measure this radiation over a relatively large area to capture a detectable signal.
- This is the reason for the small spatial resolution of data obtained by passive methods of the microwave part of the spectrum.
- Active systems record considerable development, providing data that can be used primarily for studying relief, floating ice, geomorphology, forestry, and agriculture.
- Active microwave systems can be used to obtain non-image data, information on altitude conditions, several meteorological elements, etc.

References

A dictionary of Physics. 6th ed. 2009. Oxford University Press.

Anonymous, (2023a). https://natural-resources.canada.ca/maps-tools-publications/satellite-imagery-air-photos/remote-sensing-tutorials/introduction/electromagnetic-radiation/14621

Anonymous, (2023b). https://www.circuits-diy.com/simple-electromagnetic-radiation-detector-using-tl071/

Anonymous, (2023c). http://hyperphysics.phy-astr.gsu.edu/hbase/wien.html

Browne, M. 2013. Physics for Engineering and Science. 2nd ed. McGraw Hill/Schaum, New York. 427 p. ISBN 978-0-07-161399-6

Dobrovolný, P. 1998. Remote sensing [Dálkový průzkum Země]. PřF MU v Brně, 208 p. (in Czech) https://porsec2012.incois.gov.in/documents/ITCOocean/Principles%20of%20remote%20sensing.pdf

Goody, R.M., Yung, Y.L. 1989. Atmospheric Radiation: Theoretical Basis (2nd ed.). Oxford University Press. ISBN 978-0-19-510291-8.

Herring, D. 2005. Remote Sensing. Available from: http://earthobservatory.nasa.gov/Library/RemoteSensing/

Planck, M. 1914. The Theory of Heat Radiation. 2nd ed. Masius, M. (transl.). P. Blakiston's Son & Co.

Purcell, E.M., Morin, D.J. 2013. Electricity and Magnetism. 3rd ed. Harvard University, Cambridge University Press, New York, 820p. ISBN 978-1107014022.

Siegel, R., Howell, J.R. (1992). Thermal Radiation Heat Transfer (3rd ed.). Taylor & Francis. ISBN 0-89116-271-2.

Von Laue, M. (1958). History of Physics [Dějiny fyziky]. 1st ed., Orbis, Praha 170 p. (in Czech)

3. SATELLITE SYSTEMS SUITABLE FOR AGRICULTURAL USE

Atila Bezdan, Jovana Bezdan, Boško Blagojević

With the rising global population and the imperative for sustainable development to maintain an equilibrium worldwide and meet human needs, the agricultural sector has utilized technological advancements for effective decision-making, promoting sustainable utilization of natural resources (Dakir et al., 2021). Digital agriculture has revolutionized farming, making it more efficient and more innovative (Shepherd et al., 2020). The central principle involves observing and regulating the variability in agricultural fields using intelligent technologies to enhance productivity. Various methods are now utilized in digital agriculture, including big data analytics, the Internet of Things (IoT), and remote sensing technologies (Wei et al., 2020).

Satellite Earth observation (EO) is a type of remote sensing that aims to gather data from platforms as far away as 36,000 km in space about the Earth's surface and atmosphere (Zhao e al., 2022; AHDB, 2018). The resulting data comes from various satellite missions with various sensors and mission goals rather than from a single satellite operation.

Earth observation satellites (EOS) have been in orbit since the early 1970s. There is an extensive range of satellite data accessible for various spatial/temporal resolutions and related expenses, both commercial and open-source (AHDB, 2018). Publicly-owned satellites offer openly accessible imagery with a spatial resolution of up to 10 meters, and commercial satellites provide high-resolution images of up to 0.25 meters.

The recent aggravation of the food scarcity issue prompted us to reexamine another essential function of EO-satellites, which is to help the agro-industrial sector. Modern satellite monitoring systems aid in managing crop output levels, implementing scheduled crop irrigation, and promptly detecting pest and drought threats, all of which help preserve crops (MaxPolyakov, 2023). Farmers can make better judgments regarding their livestock and crops thanks to the unparalleled precision that satellites deliver (Frąckiewicz, 2023). The use of new technologies, like those provided by satellites, holds great promise for helping growers with a variety of tasks, including determining when to harvest, forecasting in-season yields,

identifying and managing pests and diseases, understanding the water and nutrient status, organizing crop nutrition programs, and guiding in-season irrigation.

Crops were previously farmed without the assistance of space technology, but with the advent of precision agriculture and its deployment, the range of relevant information has increased dramatically. Precision farming uses the data from remote monitoring to apply differentiating fertilizer, protect plants, apply dosed irrigation, manage crops and yields, and perform numerous other farming operations that ultimately conserve resources and lower expenses by contributing to higher yields (Innovatione, 2020).

3.1. EOS agricultural measurements

Enhancing the management of crops and their inputs requires utilizing spatial information. Current crop mapping allows farmers to anticipate yields more precisely, analyze crop status, and apply inputs like fungicides, growth regulators, and fertilizer. It also gives government and research organizations a way to monitor agricultural activities. A growing amount of timely, within-season geographical information is being delivered through EO measurements (AHDB, 2018). Whether obtained via a satellite, airplane, or unmanned aerial vehicle (UAV), EO data can reveal details about the canopy surface and/or its structure (Zhao et al., 2022). Greenness and chlorophyll content, damage from disease and pests, and the presence of undesirable species like weeds are all considered when measuring the canopy's surface. Measurements of the canopy structure may include crop height, biomass, and leaf area index (LAI). Growers can utilize these many measures when combined to help guide their management choices, as shown in Figure 3.1 (AHDB, 2018).

As previously mentioned, EOS sensors measure crop reflectance and structure, which can be linked to biophysical attributes, including height, yield, growth stage, and LAI (Huete et al., 1994). It is crucial to remember that EOS rarely offers direct measurements of these biophysical characteristics; instead, it is typical to apply crop models to connect EO observations to relevant crop dynamics by utilizing EOS data in a data science method (AHDB, 2018).

Much research has gone into yield prediction in agriculture, and several models have been created for various crops, including potatoes, wheat, maize, and sugar beet (Sharifi, 2021; Rembold et al., 2013). Several direct ground measures of the crop are typically taken throughout the year to track productivity. These measurements include the tiller number, leaf area index, crop height, and weed infestation. Regression against previously measured yield data is

typically used to anticipate yield afterward. Yield models progressively incorporate essential characteristics that can be calculated from EO, such as vegetation indices that infer LAI or weed infestations from high spatial resolution data. In this case, the primary benefit of EO is its capacity to quickly evaluate parameters over far wider spatial areas than can be observed on the ground (AHDB, 2018). More complex numerical agricultural models that estimate crop biomass, health, and yield using agro-meteorological parameters (such as temperature, rainfall, radiation, crop type, soil type, and nutrient availability) can also be integrated with EO data.

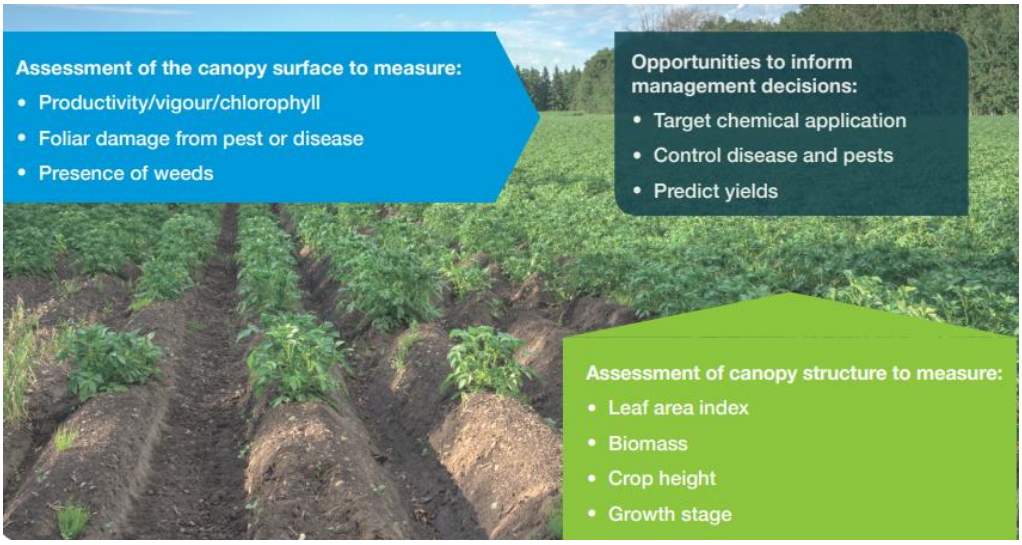

Figure 3.1 Understanding of crops through EO. Image credit: Satellite Applications Catapult (AHDB, 2018)

3.2. EOS for monitoring environmental parameters

The capacity of EO to continuously and routinely monitor large areas of land and atmosphere gives it its power. Various EOS sensors can be utilized to track common environmental factors, such as vegetation, hydrological parameters, land/soil properties, and atmospheric variables that are employed in an environmental impact assessment. Table 3.1 gives an evaluation summary of EOS's suitability for monitoring environmental parameters (AHDB, 2018).

Table 3.1 Suitability of earth observation satellites for monitoring environmental parameters

Measurement	Description	Sensor(s)	Ground resolution	Temporal resolution	Application considerations
Aerosol monitoring (including water vapour)	Measure changes in composition of key atmospheric gases including nitrogen dioxide, sulphur dioxide, ozone, carbon monoxide and carbon dioxide	Very low resolution multispectral (eg MODIS, Sentinel-4/5/5P; SMM/I, AVHRR or MERIS from LEO platforms or SEVIRI from GEO)	100s of metres to kilometres	1–2 days	There is a general trade-off between spatial and temporal resolution. While satellites in geostationary orbit stay in the same place relative to Earth, giving a high temporal resolution and a low ground resolution, satellites in polar/ sun-synchronous orbit scan across the entire Earth's surface
Dust monitoring	Routine measurements of PM2.5 and PM10 for regional-scale analysis	Medium resolution visible or multispectral (eg GOES, Landsat TM)	30 m to 100s of metres	15 minutes – 2 weeks	
Land surface temperature	Local changes to land surface and atmosphere (eg land cover change, dust presence) can alter land surface temperature affecting local habitats and ecosystems	Thermal sensors (eg Landsat TM/ ETM+, Landsat TIIRS, ASTER, MODIS and AVHRR)	90 m–100s of metres	1–2 days or 8 days depending on the sensor	
Surface water	Remote sensing can be used to identify water bodies	High/Medium resolution multispectral sensors and SAR (eg Sentinel 1A/B, Sentinel 2)	0.25 m–30 m	6–12 days	Most effective on larger water bodies such as major lakes and rivers. Satellite information can only be used to inform water quality for a limited number of parameters (ie turbidity, and presence of algae blooms). As such, this application is likely only complementary to in-situ monitoring with current technology Commercial alternatives such as Cosmo-SkyMed can give spatial resolution down to 1m and a near-daily revisit
Surface water quality	EO can be used to monitor water quality	Low resolution narrowband multispectral (eg MODIS)	500 m	1–2 days	
Ground water	EO cannot be used to measure directly subsurface groundwater. Total water storage changes over large scales can be estimated using in-situ observations coupled with satellite observations of gravity	GRACE/GOCE only (Microwave/gravity gradiometer)	300–400 km	Monthly	Numerous techniques do exist to map proxy indicators of groundwater presence, such as land cover, soil moisture etc. Modelling from satellite-derived products including DEMs, soil maps, and geology maps can also provide estimation of groundwater potential
Soil moisture	Satellites can be used to derive regional soil moisture levels	High/Medium resolution SAR (eg SMOS)	35 km	3 days	Regional soil mapping typically still requires complementary field mapping to identify specific soil types, but EO-based modelling techniques can allow rapid wider delineation. See also Hazards section for benefit of monitoring soil moisture
Soil type	Satellites can be used for monitoring exposed soil, differentiating between broad exposed soil types				

3.3. Most commonly used satellite systems for agricultural use

- Sentinel 2

Sentinel 2 mission (Figure 3.2) was launched within the European Commission's Copernicus program on June 23, 2015. It was made to deliver a large number of data and images. The satellite (Image 8.) is equipped with multispectral sensors for capturing Sentinel 2 images with a resolution from 10 to 60 meters in the visible, near-infrared, and short-wave

infrared spectrum, including 13 spectral channels, which ensures the capture of differences in vegetation state, including temporal changes. Also, it minimizes the impact on the quality of atmospheric photography. Four channels are at 10 m (B2, B3, B4, and B8), six at 20 m (B5, B6, B7, B8A, B11, and B12) and three channels at a spatial resolution of 60 m (Table 3.2). The orbit is at an average height of 785 km, and two satellites in the mission allow repeated examinations every 5 days at the equator and every 2 - 3 days at mid-geographical latitudes. The Sentinel 2 mission consists of two identical satellites (Sentinel 2A and Sentinel 2B) positioned 180° apart. Sentinel 2A was launched on June 23, 2015, and Sentinel 2B on March 7, 2017.

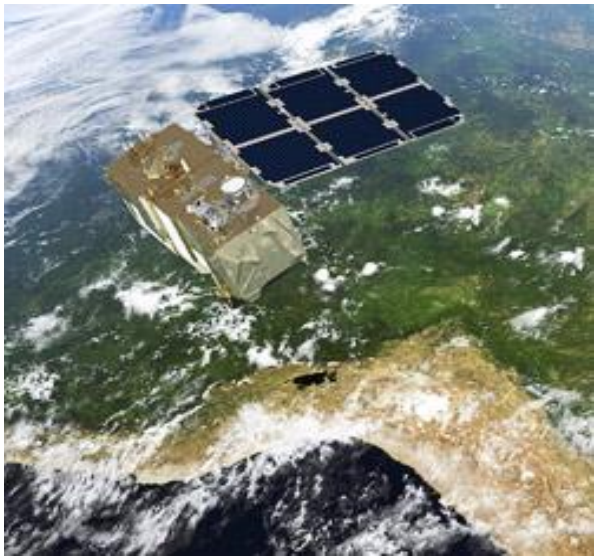

Figure 3.2 Sentinel 2 Satellite (Anonymous, 2023a)

Copernicus is the European Commission's Earth Observation program's new name, formerly GMES (Global Monitoring for Environment and Security). The new name was announced on December 11, 2012, by Antonio Tajani, Vice-President of the EC (European Commission), during the Competitiveness Council.

Sentinel 2 is a multispectral operational visual mission within the Copernicus program, jointly implemented by the EC (European Commission) and ESA (European Space Agency), for global land observation (data on vegetation, soil, and water coverage for terrestrial, inland waterways, and coastal areas, as well as for the correction of data on atmospheric absorption and distortion) at high resolution with a high revisit capability to ensure more excellent continuity of data previously provided by SPOT-5 and Landsat-7.

Table 3.2 Spectral bands for the Sentinel-2 sensors

Sentinel-2 bands	Sentinel-2A		Sentinel-2B		
	Central wavelength (nm)	Bandwidth (nm)	Central wavelength (nm)	Bandwidth (nm)	Spatial resolution (m)
Band 1 – Coastal aerosol	442.7	21	442.2	21	60
Band 2 – Blue	492.4	66	492.1	66	10
Band 3 – Green	559.8	36	559.0	36	10
Band 4 – Red	664.6	31	664.9	31	10
Band 5 – Vegetation red edge	704.1	15	703.8	16	20
Band 6 – Vegetation red edge	740.5	15	739.1	15	20
Band 7 – Vegetation red edge	782.8	20	779.7	20	20
Band 8 – NIR	832.8	106	832.9	106	10
Band 8A – Narrow NIR	864.7	21	864.0	22	20
Band 9 – Water vapour	945.1	20	943.2	21	60
Band 10 – SWIR – Cirrus	1373.5	31	1376.9	30	60
Band 11 – SWIR	1613.7	91	1610.4	94	20
Band 12 – SWIR	2202.4	175	2185.7	185	20

Sentinel 2 is part of the Copernicus program, the most extensive individual Earth observation program, led by the European Commission in partnership with the European Space Agency. Each of the Sentinel 2 mission satellites has an optical instrument capable of capturing in 13 spectral bands: four channels at 10 m, six channels at 20 m, and three channels at 60 m spatial resolution. The width of the orbital swath is 290 kilometers. Sentinel 2 continuously collects images from two Earth observation satellites that provide images for any location worldwide every 5 to 7 days.

The mission supports a wide range of services and applications, such as agricultural monitoring, emergency management, land classification, and water quality.

- Landsat 9 (https://landsat.gsfc.nasa.gov/satellites/landsat-9)

Since 1972, Landsat satellites (Figure 3.3) have continuously recorded data about the Earth's surface, coastal zones, coral reefs, etc. The Landsat program was created in collaboration between the US Geological Survey (USGS) and the National Aeronautics and Space Administration (NASA) to capture images of the Earth's surface from space.

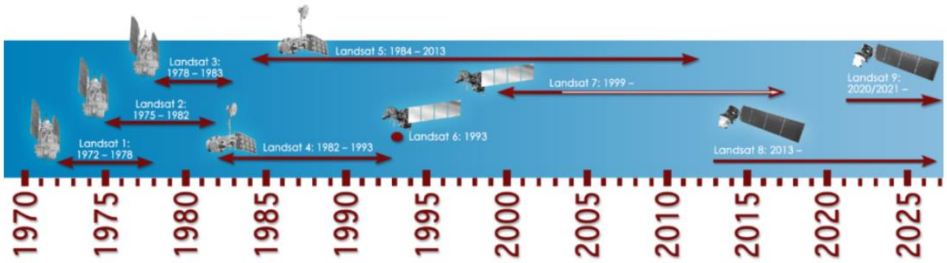

Figure 3.3 A Landsat Timeline (Anonymous, 2023b)

The U.S. Geological Survey (USGS) and the National Aeronautics and Space Administration (NASA) collaborated to create Landsat 9, which carries on the vital function that Landsat played in repeating worldwide observations for monitoring, comprehending, and managing Earth's natural resources.

The Landsat 9 instrument system is an enhanced version of the Landsat 8 instrument, which is now gathering data superior to that of prior-generation Landsat satellites in terms of radiometric and geometric quality.

The Thermal Infrared Sensor 2 (TIRS-2) and Operational Land Imager 2 (OLI-2) are the satellite's scientific instruments. The TIRS-2 measures the heat, or thermal infrared radiation, released from the Earth's surface. The OLI–2 records the Earth's surface observations in the visible, near-infrared, and shortwave-infrared bands. The mission design life of OLI and TIRS is five years, whereas the spacecraft's consumables last for more than ten years.

Higher radiometric resolution for OLI-2 (14-bit quantization up from 12-bits for Landsat 8) is one of Landsat 9's advancements. This allows sensors to pick up on more minute details, particularly over darker regions like dense woods or bodies of water. Landsat 9 has a greater radiometric resolution and can distinguish 16,384 colors of a particular wavelength. In contrast, Landsat 7's 8-bit resolution allows it to distinguish only 256 hues, while Landsat 8's 12-bit data allows it to detect 4,096 shades. Better atmospheric correction and more precise surface temperature measurements are made possible by TIRS-2's substantial reduction of stray light compared to the Landsat 8 Thermal Infrared Sensor (TIRS) and the enhancement of OLI-2.

OLI-2, or Operational Land Imager 2

Landsat 8's OLI was replicated in the design of OLI-2, which offers imagery that is compatible with Landsat's past spectral, spatial, radiometric, and geometric characteristics.

Except for the panchromatic band, which has a GSD of 15 meters, OLI-2 will give data for nine spectral bands with a maximum ground sampling distance (GSD), both in-track and cross-track, of 30 meters (m). To guarantee radiometric stability and precision, OLI-2 offers both internal calibration sources and the capability to carry out solar and lunar calibrations. Boulder, Colorado-based Ball Aerospace is the designer of OLI-2.

Nine bands of the spectrum:

- Band 1: Aerosol Visible Coastal (0.43 - 0.45 µm) 30 m
- Visible Blue Band 2 (0.450 - 0.51 µm) 30 m
- Visible Green Band 3 (0.53 - 0.59 µm) 30 m
- Red Band 4 (0.64–0.67 µm) 30 m
- Near-Infrared Band 5 (0.85 - 0.88 µm) 30 m
- SWIR Band 6 (1.57 - 1.65 µm) 30 m
- SWIR 2, Band 7 (2.11 - 2.29 µm) 30 m
- Panchromatic Band 8 (PAN): 0.50 - 0.68 µm 15.
- Cirrus Band 9 (1.36 - 1.38 µm) 30 m
- TIRS-2: Thermal Infrared Sensor

TIRS-2: Thermal Infrared Sensor

Using the same technology used for TIRS on Landsat 8, Landsat 9's Thermal Infrared Sensor 2 (TIRS-2) measures thermal radiance emitted from the land surface in two thermal infrared bands. However, TIRS-2 is an improved version of Landsat 8's TIRS in terms of instrument risk class and design to minimize stray light. TIRS-2 offers two spectrum bands with a maximum ground sampling distance of 100 meters (328 feet) for each band, both in-track and cross-track. TIRS-2 has space view capabilities in addition to an internal blackbody calibration source. NASA's Goddard Space Flight Center in Greenbelt, Maryland, is responsible for designing TIRS-2.

Two bands of spectrum:

- 100-meter Band 10 TIRS 1 (10.6 - 11.19 µm)
- 100-meter Band 11 TIRS 2 (11.5 - 12.51 µm)

Spectral Sensing of Cropland

It should be highlighted that satellite monitoring encompasses more than just the customary optical satellite observations of crop development. The technique of remote satellite sensing the earth's surface using various types of sensors is the most significant resource for precision farming. This kind of EO provides images of the Earth's surface in different electromagnetic spectrums. These spectra and a standard optical camera are invisible to the naked eye, but they show much important information about the vegetation process.

The following text briefly describes some of the most commonly used satellite-based indices.

Satellite-based indices

- NDVI

The Normalized Difference Vegetation Index (NDVI) is the most often used metric for determining the degree of greening from orbit (DeFries and Townshend, 1994; Carlson and Ripley, 1997; Pettorelli, 2005). The index shows the degree of greening of the scanned surface. The NDVI indicator, which is based on spectrum analysis, makes it possible to observe the details of the vegetation process that are connected to illnesses, dryness, and other unfavorable circumstances that lower the degree of greening (MaxPolyakov, 2023).

The method by which plants absorb visible light, known as photosynthesis, was visually defined and served as the foundation for the technology that first appeared in the 1980s (MaxPolyakov, 2023). During photosynthesis, plants intensively absorb light, which causes them to reflect a lot of near-infrared light (NIRB) into the surrounding air. The NDVI index, developed based on our understanding of the various infrared light reflections, enabled us to use remote sensing techniques to pinpoint the greenest regions (Figure 3.4-3.5).

The maximum value of one on the NDVI index represents the glow reflected from healthy, densely growing plants. The index ranges from -1 to 1. The formula for calculating NDVI is:

$$\mathrm{NDVI} = \frac{\mathrm{NIR} - \mathrm{RED}}{NIR + RED}$$

Dense vegetation typically has NDVI values from 0.3 to 0.8. Clouds and snow cover have negative NDVI values. Water bodies (oceans, seas, lakes, and rivers) have a low reflection in both spectral ranges, so the NDVI for water surfaces has a very low or negative positive value. Bare soil has a minimal review in the near-infrared part, so the NDVI value is positive, ranging from 0.1 to 0.2. These numerical values are typically represented on the spectral picture as specific colors: green denotes a sufficient level of plant health, while yellow and red indicate the presence of sick or withering leaves (Figure 3.4-3.5).

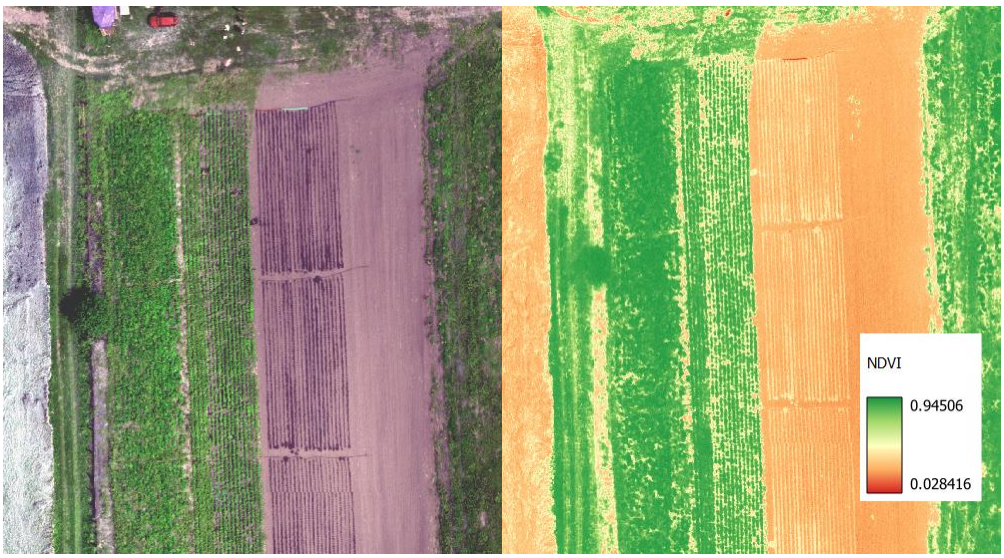

Figure 3.4 Agricultural plots shot with conventional RGB camera (left) and with the NDVI (right)

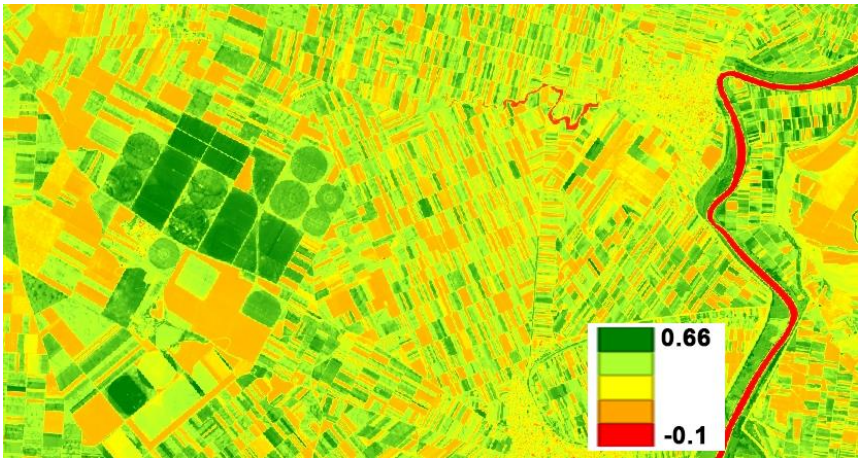

Figure 3.5. Example of NDVI image

Note that the NDVI is not a universal vegetation index that can be applied to every aspect of farming. Numerous more indices are available to assist in analyzing a variety of vegetative cycle-related data depending on different characteristics. Other indices may be used to identify crops based on their spectral imprint, measure leaf chlorophyll levels and provide an area index, detect pest and disease outbreaks promptly, and offer information on the kind of soil and moisture saturation.

-SAVI

The Soil-Adjusted Vegetation Index (SAVI) index represents a modification of NDVI to eliminate the influence of the atmosphere and soil. It attempts to minimize soil brightness influences using a soil-brightness correction factor. SAVI is often used in arid regions with low vegetative cover (Huete, 1988). It is calculated using the following formula:

$$\text{SAVI} = \frac{(1+L)(NIR-RED)}{NIR+RED+L}$$

The L value varies based on the extent of green vegetation cover. Typically, in regions with no green vegetation, L equals 1; in zones with moderate green vegetation, L is set at 0.5; and in areas with extremely dense vegetation cover, L is 0 (making it analogous to the NDVI method). The range of values produced by this index spans from -1.0 to 1.0. In the example in Figure 3.6 and in the case of NDVI, the difference between the presence of vegetation (green color) and the fragile presence of vegetation (red color) is clearly visible.

- EVI

The Enhanced Vegetation Index (EVI) was developed to optimize the vegetation signal and improve the sensitivity to improve vegetation monitoring through a de-coupling of the canopy background signal and atmosphere influences (Liu and Huete, 1995). EVI is calculated as follows:

$$\text{EVI} = G\frac{NIR-R}{\text{NIR}+\text{C}_1\text{R}-\text{C}_2\text{B}+\text{L}}$$

Where:

- NIR, Red, and Blue are atmospherically-corrected surface reflectances;
- L is the canopy background adjustment that addresses non-linear, differential NIR and red radiant transfer through a canopy;

- C1, C2 are the coefficients of the aerosol resistance term, which uses the blue band to correct for aerosol influences in the red band.;
- G is a gain factor.

The coefficients' Usual values are $C_1 = 6$; $C_2 = 7,5$; $G = 2,5$; $L = 1$.

The NDVI index is sensitive to chlorophyll, while the EVI (Figure 3.7) index is more sensitive to the structural variation of vegetation, such as vegetation type and plant physiognomy. These two indices are complementary and are often used together in the study of changes in the biophysical characteristics of vegetation. The value of the EVI index ranges from -1 to +1, and the usual vegetation values are from 0.2 to 0.8. EVI is most often used to estimate biomass, determine biophysical characteristics of vegetation, and quantify evapotranspiration or water use efficiency.

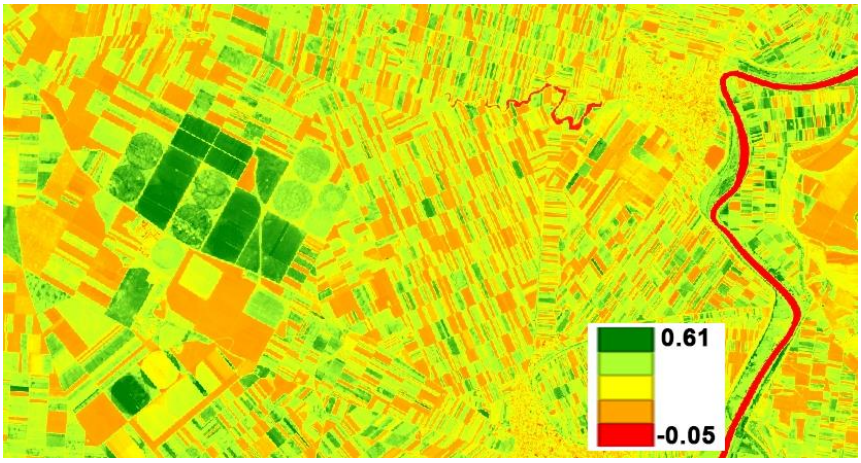

Figure 3.6 Example of SAVI image

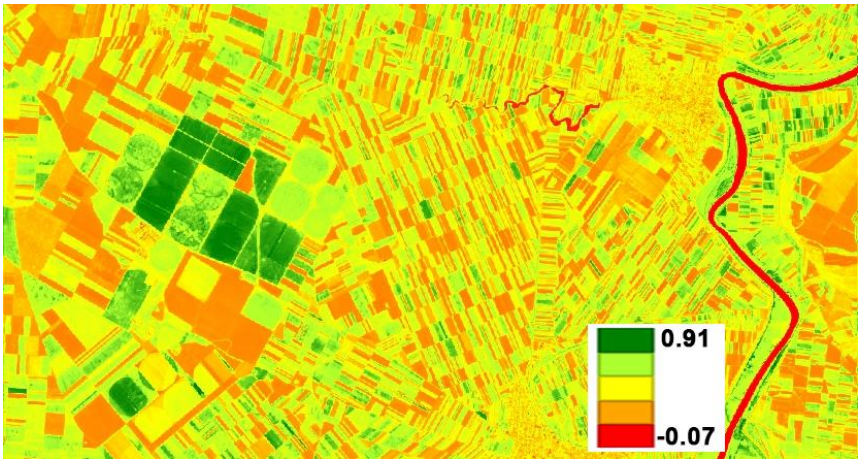

Figure 3.7 Example of EVI image

- NDWI (McFeeters, 1996)

The Normalized Difference Water Index (NDWI) is utilized to higlight open water areas in satellite imagery, enabling the clear distinction of water bodies from surrounding soil and vegetation. Introduced by McFeeters in 1996, the NDWI index is primarily employed nowadays for detecting and tracking subtle variations in the water content of bodies of water. By leveraging the NIR (near-infrared) and GREEN (visible green) spectral bands, the NDWI (Figure 3.8) effectively highlights water bodies in satellite imagery. However, a limitation of this index is its sensitivity to artificial structures, potentially resulting in overestimating water body areas. NDWI is calculated as follows:

$$\mathrm{NDWI} = \frac{\mathrm{Green} - \mathrm{NIR}}{\mathrm{Green} + \mathrm{NIR}}$$

The NDWI values correspond to the following ranges:

- +0,2 – 1.0 Water surface,
- +0.0 – 0,2 Flooding, humidity,
- -0,3 – 0.0 Moderate drought, surfaces not containing water,
- -1.0 – -0.3 Drought, surfaces not containing water.

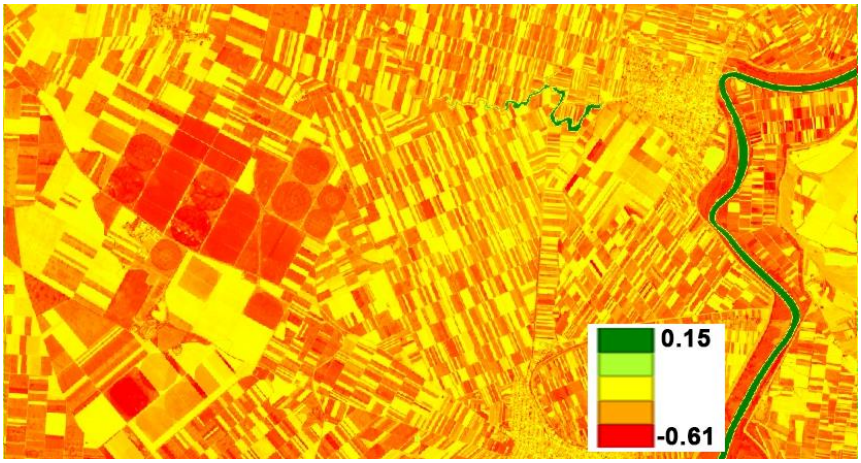

Figure 3.8 Example of NDWI *(McFeeters, 1996)* image

- NDWI (Gao, 1996)

The Normalized Difference Water Index (NDWI) uses the NIR-SWIR (near-infrared and short-wave infrared) combination to enhance the presence of water in the leaves of plants. NDWI is widely recognized as a reliable indicator of plant water content, making it an effective

measure of plant water stress. NDWI is used to monitor changes in the water content of leaves, using near-infrared (NIR) and short-wave infrared (SWIR) wavelengths, as proposed by Gao in 1996. Reflectance in the SWIR spectrum indicates alterations in vegetation's water content and the porous mesophyll structure within plant canopies. Meanwhile, NIR reflectance is influenced by the internal structure of leaves and their dry matter content, but it remains unaffected by water content (European Commission, 2011).

NDWI is calculated as follows:

$$\text{NDWI} = \frac{\text{NIR} - \text{SWIR}}{\text{NIR} + \text{SWIR}}$$

The NDWI (Figure 3.9) values vary between -1 to +1, depending on the leaf water content and the vegetation type and cover. High values of NDWI correspond to high vegetation water content and high vegetation fraction cover. Low NDWI values correspond to low vegetation water content and low vegetation fraction cover. In periods of water stress, NDWI will decrease.

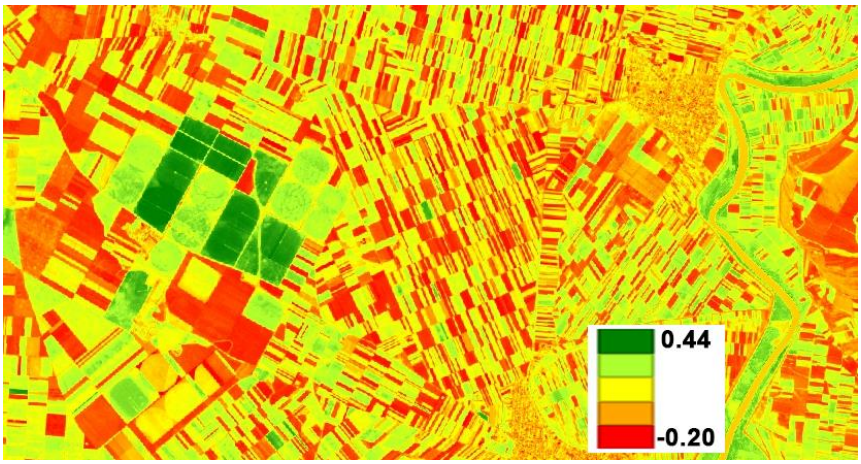

Figure 3.9 Example of NDWI *(Gao, 1996)* image

Conclusion

Controlling the entire farming process, from the seeding campaign to the harvest, is now feasible thanks to satellite monitoring. The increasing availability of satellite data and the expanding number of organizations offering it both significantly affect the evolution of successful EO technology integration in farms. Technological advancements in satellite

monitoring have also added to the growing appeal of EO: new camera types may provide farmers with incredibly clear views, making it harder to distinguish between high-resolution aerial photography and satellite imagery (MaxPolyakov, 2023).

It is becoming increasingly apparent that the technology associated with precision farming will give rise to an entirely new, more intelligent, and cost-effective way of farming that will enable you to grow more and better while consuming fewer resources. It will be impossible to picture a farmer without connection with an orbiting satellite shortly, just as it was impossible to imagine one without a plow or a combine fifty years ago.

References

AHDB, (2018). https://projectblue.blob.core.windows.net/media/Default/Imported%20Publication%20Docs/SatellitesForAgriculture1825_181217_WEB.pdf

Anonymous (2023a).https://landsat.gsfc.nasa.gov/article/a-landsat-timeline/)

Anonymous (2023b). www.sentinel-hub.com/sentinel-2)

Carlson, T.N. and Ripley, D.A., (1997). On the relation between NDVI, fractional vegetation cover, and leaf area index. *Remote sensing of Environment*, *62*(3), pp.241-252.

Dakir, A., Zahra, B.F. and Omar, A.B., (2021). Optical satellite images services for precision agricultural use: a review. *Remote Sensing*, *4*, p.18.

DeFries, R.S. and Townshend, J.R.G., (1994). NDVI-derived land cover classifications at a global scale. *International journal of remote sensing*, *15*(17), pp.3567-3586.

European Commission. NDWI: Normalized Difference Water Index. (2011). Version 1. DESERT Action - LMNH Unit. Accessed March 13, 2019. Available at: http://edo.jrc.ec.europa.eu/documents/factsheets/factsheet_ndwi.pdf

Frąckiewicz, (2023). https://ts2.space/en/the-use-of-satellites-in-precision-agriculture-and-farming/

Gao, B.C., (1996). NDWI—A normalized difference water index for remote sensing of vegetation liquid water from space. *Remote sensing of environment*, *58*(3), pp.257-266.

Huete, A., Justice, C. and Liu, H., (1994). Development of vegetation and soil indices for MODIS-EOS. *Remote Sensing of Environment*, *49*(3), pp.224-234.

Huete, A.R., (1988). A soil-adjusted vegetation index (SAVI). *Remote sensing of environment*, *25*(3), pp.295-309.

Innovatione, (2020). https://innovatione.eu/en/2020/07/15/remote-sensing-satellite-applications-in-agriculture/

Liu, H.Q. and Huete, A., (1995). A feedback based modification of the NDVI to minimize canopy background and atmospheric noise. *IEEE transactions on geoscience and remote sensing*, *33*(2), pp.457-465.

MaxPolyakov, (2023). https://maxpolyakov.com/satellite-uses-in-farming-and-agriculture/

McFeeters, S.K., (1996). The use of the Normalized Difference Water Index (NDWI) in the delineation of open water features. *International journal of remote sensing*, *17*(7), pp.1425-1432.

Pettorelli, N., Vik, J.O., Mysterud, A., Gaillard, J.M., Tucker, C.J. and Stenseth, N.C., (2005). Using the satellite-derived NDVI to assess ecological responses to environmental change. *Trends in ecology & evolution*, *20*(9), pp.503-510.

Rembold, F., Atzberger, C., Savin, I. and Rojas, O., (2013). Using low resolution satellite imagery for yield prediction and yield anomaly detection. *Remote Sensing*, *5*(4), pp.1704-1733.

Sharifi, A., 2021. Yield prediction with machine learning algorithms and satellite images. *Journal of the Science of Food and Agriculture*, *101*(3), pp.891-896.

Shepherd, M., Turner, J. A., Small, B., & Wheeler, D. (2020). Priorities for science to overcome hurdles thwarting the full promise of the 'digital agriculture'revolution. Journal of the Science of Food and Agriculture, 100(14), 5083-5092.

Wei, M. C. F., Maldaner, L. F., Ottoni, P. M. N., & Molin, J. P. (2020). Carrot yield mapping: a precision agriculture approach based on machine learning. Ai 1: 229–241.

Zhao, Q., Yu, L., Du, Z., Peng, D., Hao, P., Zhang, Y. and Gong, P., (2022). An overview of the applications of earth observation satellite data: impacts and future trends. *Remote Sensing*, *14*(8), p.1863.

4. UAV SYSTEM SUITABLE FOR AGRICULTURAL USE

Dr. Emre Tunca

Agriculture plays a vital role in global food security and economic development. Advancements in technology, such as UAV systems, can revolutionize agricultural practices (Istiak et al., 2023; Kim et al., 2019). Unmanned Aerial Vehicles (UAVs) represent a significant technological advancement in the field of agriculture, increasing farming efficiency and sustainability (Aboutalebi et al., 2020). Since agriculture has always been a cornerstone of global food security and economic stability, it has always been open to new approaches to enhance productivity and resource efficiency (Gao et al., 2020). In this context, UAV has emerged as a powerful tool that provides detailed and rapid data collection capabilities that are superior to the traditional methods (Stanton et al., 2017; Tunca et al., 2018a).

The application of UAVs in agriculture is diverse and impactful (Hassan et al., 2019; Tunca et al., 2018a). These systems are primarily used for precision farming (Candiago et al., 2015), crop monitoring (Tunca et al., 2018a), disease detection (Shahi et al., 2023), and irrigation management (Tunca, 2023). By providing high-resolution aerial imagery, UAVs allow farmers to closely monitor crop health, assess soil conditions, and manage resources more effectively (Chang et al., 2017). This level of precision is particularly beneficial in optimizing the application of water, fertilizers, and pesticides, leading to increased yield and reduced environmental impact (Gao et al., 2023; Harkel et al., 2020; Messina and Modica, 2020; Tunca et al., 2018b).

The benefits of UAVs in agriculture are multi-fold. As detailed by Tunca et al. (2018a), enhanced monitoring capabilities provide farmers with insights into crop health at a resolution unattainable by traditional methods. This high-resolution data is instrumental in resource optimization, reducing costs and environmental footprint, as Xie et al. (2021) discussed. Moreover, Istiak et al. (2023) highlighted the efficiency of UAVs in large-scale operations, where their ability to cover vast areas quickly is unmatched.

However, integrating UAVs into agricultural practices is not free from challenges. Regulatory constraints, as discussed by Cho (2013), pose significant challenges in UAV

deployment. Technical limitations, including battery life and payload capacity, have been identified by Mohsan et al. (2022) as key areas needing improvement. The challenge of managing and processing the large volumes of data generated by UAVs is another aspect that has been brought to light by Alsamhi et al. (2022). Furthermore, the economic aspect, particularly the cost of acquiring and maintaining UAV systems, is a concern for smaller farms, as stated by Tunca et al. (2023).

In conclusion, adopting UAV technology in agriculture is a significant step towards more efficient and sustainable farming practices. While the potential benefits are substantial, as evidenced by the existing literature, addressing the technical, regulatory, and economic challenges is crucial for maximizing their impact. The ongoing research and development in this field, as documented by Nassar et al. (2022) and Hou et al. (2021), continue to push the boundaries of what UAVs can achieve in agriculture, promising an even more innovative and productive future for the sector.

References

Aboutalebi, M., Torres-Rua, A.F., McKee, M., Kustas, W.P., Nieto, H., Alsina, M.M., White, A., Prueger, J.H., McKee, L., & Alfieri, J. (2020). Incorporation of unmanned aerial vehicle (UAV) point cloud products into remote sensing evapotranspiration models. *Remote Sensing, 12*, 50

Alsamhi, S.H., Shvetsov, A.V., Kumar, S., Hassan, J., Alhartomi, M.A., Shvetsova, S.V., Sahal, R., & Hawbani, A. (2022). Computing in the sky: A survey on intelligent ubiquitous computing for uav-assisted 6g networks and industry 4.0/5.0. *Drones, 6*, 177

Candiago, S., Remondino, F., De Giglio, M., Dubbini, M., & Gattelli, M. (2015). Evaluating multispectral images and vegetation indices for precision farming applications from UAV images. *Remote Sensing, 7*, 4026-4047

Chang, A., Jung, J., Maeda, M.M., & Landivar, J. (2017). Crop height monitoring with digital imagery from Unmanned Aerial System (UAS). *Computers and Electronics in Agriculture, 141*, 232-237

Cho, G. (2013). Unmanned aerial vehicles: Emerging policy and regulatory issues. *Journal of Law, Information and Science, 22*, 201-236

Gao, R., Nassar, A., Aboutalebi, M., Torres-Rua, A.F., Prueger, J.H., McKee, L., Alfieri, J.G., Hipps, L., Nieto, H., & White, W.A. (2020). Grapevine Leaf Area Index Estimation with

Machine Learning and Unmanned Aerial Vehicle Information. In, *AGU Fall Meeting Abstracts* (pp. H008-0012)

Gao, R., Torres-Rua, A.F., Nieto, H., Zahn, E., Hipps, L., Kustas, W.P., Alsina, M.M., Bambach, N., Castro, S.J., & Prueger, J.H. (2023). ET Partitioning Assessment Using the TSEB Model and sUAS Information across California Central Valley Vineyards. *Remote Sensing, 15*, 756, https://doi.org/10.3390/rs15030756

Harkel, J., Bartholomeus, H., & Kooistra, L. (2020). Biomass and crop height estimation of different crops using UAV-based LiDAR. *Remote Sensing, 12*, 17

Hassan, M.A., Yang, M., Fu, L., Rasheed, A., Zheng, B., Xia, X., Xiao, Y., & He, Z. (2019). Accuracy assessment of plant height using an unmanned aerial vehicle for quantitative genomic analysis in bread wheat. *Plant Methods, 15*, 1-12

Hou, M., Tian, F., Ortega-Farias, S., Riveros-Burgos, C., Zhang, T., & Lin, A. (2021). Estimation of crop transpiration and its scale effect based on ground and UAV thermal infrared remote sensing images. *European Journal of Agronomy, 131*, 126389,

Istiak, M.A., Syeed, M.M., Hossain, M.S., Uddin, M.F., Hasan, M., Khan, R.H., & Azad, N.S. (2023). Adoption of Unmanned Aerial Vehicle (UAV) imagery in agricultural management: A systematic literature review. *Ecological Informatics*, 102305

Kim, J., Kim, S., Ju, C., & Son, H.I. (2019). Unmanned aerial vehicles in agriculture: A review of perspective of platform, control, and applications. *IEEE Access, 7*, 105100-105115

Messina, G., & Modica, G. (2020). Applications of UAV thermal imagery in precision agriculture: State of the art and future research outlook. *Remote Sensing, 12*, 1491, https://doi.org/10.3390/rs12091491

Mohsan, S.A.H., Khan, M.A., Noor, F., Ullah, I., & Alsharif, M.H. (2022). Towards the unmanned aerial vehicles (UAVs): A comprehensive review. *Drones, 6*, 147

Nassar, A., Torres-Rua, A., Hipps, L., Kustas, W., McKee, M., Stevens, D., Nieto, H., Keller, D., Gowing, I., & Coopmans, C. (2022). Using Remote Sensing to Estimate Scales of Spatial Heterogeneity to Analyze Evapotranspiration Modeling in a Natural Ecosystem. *Remote Sensing, 14*, 372

Shahi, T.B., Xu, C.-Y., Neupane, A., & Guo, W. (2023). Recent Advances in Crop Disease Detection Using UAV and Deep Learning Techniques. *Remote Sensing, 15*, 2450

Stanton, C., Starek, M.J., Elliott, N., Brewer, M., Maeda, M.M., & Chu, T. (2017). Unmanned aircraft system-derived crop height and normalized difference vegetation index metrics for sorghum yield and aphid stress assessment. *Journal of Applied Remote Sensing, 11*, 026035

Tunca, E. (2023). Evaluating the performance of the TSEB model for sorghum evapotranspiration estimation using time series UAV imagery. *Irrigation Science*, 1-18,

Tunca, E., Köksal, E.S., Çetin, S., Ekiz, N.M., & Balde, H. (2018a). Yield and leaf area index estimations for sunflower plants using unmanned aerial vehicle images. *Environmental Monitoring and Assessment, 190*, 1-12

Tunca, E., Köksal, E.S., Çetin, S., Ekiz, N.M., & Balde, H. (2018b). Yield and leaf area index estimations for sunflower plants using unmanned aerial vehicle images. *Environmental Monitoring and Assessment, 190*, 1-12, https://doi.org/10.1007/s10661-018-7064-x

Tunca, E., Köksal, E.S., & Taner, S.Ç. (2023). Calibrating UAV thermal sensors using machine learning methods for improved accuracy in agricultural applications. *Infrared Physics & Technology, 133*, 104804

5. VEGETATION MAPPING AND MONITORING

Dr. Sakine Çetin Taner

Assessing and monitoring the condition of the Earth's surface is a fundamental requirement of global change research (Lambin et al. 2001; Jung et al. 2006; Xie e al., 2008). To better evaluate the environment and ecosystem, it is necessary to obtain regularly or annually updated data on changes in vegetation status (Knight et al. 2006; Xie e al., 2008). Vegetation canopy defines the main landscape features of nature, and vegetation health is an indicator of environmental processes occurring in soil-vegetation systems (Lemenkova, 2021). Classification and vegetation mapping are essential for natural resources management and global climate change (Xiao et al., 2004).

It is often impossible to determine the vegetation covers using traditional methods (e.g., field surveys, literature reviews, map interpretation, and data analysis) because they are time-consuming, outdated, and often too expensive. Remote sensing techniques provide a practical and economical tool for studying vegetation status and changes, especially over large areas (Langley et al. 2001; Nordberg and Evertson 2003; Xie et al., 2008). Vegetation mapping using remote sensing technology is used for different purposes such as plant classification, estimation of crop planting areas, canopy chlorophyll density, leaf area index, and yield estimation (Broge and Leblanc, 2001; Shanmugapriya et al., 2019; Lemenkova, 2021).

Spektral Vegetation indices (VI_s) are used to analyze vegetation distribution and healthiness. VIs differ in terms of algorithm approach and spectral band composition (extent of the data range) (Lemenkova, 2021). The Normalised Difference Vegetation Index (NDVI) proposed by Rouse et al. (1974) is widely used in the literature. The Soil Adjusted Vegetation Index (SAVI) proposed by Huete (1988) is an example of a vegetation index that limits the effect of soil on vegetation. Spektral vegetation indices such as Enhanced Vegetation Index (EVI), Simple Ratio (SR), vegetation condition index (VCI), and leaf area index (LAI) have also been applied in different studies and fields in the literature (Pereira et al., 2011; Peng et al., 2011; Zambrano et al., 2016; Hossain et al., 2017; Hashimoto et al., 2019; Hama et al., 2021; Yan et al., 2021; Alahacoon et al., 2021). Some spectral vegetation indices (NDVI, SAVI, Renormalized Difference Vegetation Index (RDVI), Optimized Soil Adjusted Vegetation Index

(OSAVI) etc.) have been used with different parameters in some approaches for estimating plant water status (Rossini et al., 2013; Panadiga et al., 2014; Dangwal et al., 2015; Katsoulas et al. 2016; Magney et al., 2016; Evanidi et al., 2017; Ihuoma and Madramootoo 2017, 2019). The basic equations of vegetation indices used for agricultural purposes are given in Table 1.

Table 5.1 Some examples of vegetation indices used in the agricultural sector

Index	Equation	References
The Normalized Difference Vegetation Index (NDVI)	$\frac{NIR - RED}{NIR + RED}$	Rouse et al. (1974)
The Soil Adjusted Vegetation Index (SAVI)	$(1 + L) \times \frac{(NIR - RED)}{(L + NIR + RED)}$	Huete (1988)
Enhanced Vegetation Index (EVI)	$G \times \frac{(NIR - RED)}{NIR + (C1 \times RED - C2 \times BLUE) + L}$	Liu and Huete, (1995)
Simple Ratio (SR)	$\frac{NIR}{RED}$	Jordan (1969)
Normalized Difference Water Index (NDWI)	$\frac{NIR - SWIR}{NIR + SWIR}$	Gao (1996)
Land Surface Water Index (LSWI)	$\frac{NIR - SWIR}{NIR + SWIR}$	Chandrasekar et al., (2010)
Vegetation Condition Index (VCI)	$100 \times \frac{NDVI - NDVI_{min}}{NDVI_{max} + NDVI_{min}}$	Kogan (1995)
Leaf Area Index (LAI)	$-\frac{\ln((0{,}69 - SAVI)/0{,}59}{0{,}91}$	Bastiaanssen (1998)
(DVI)	NIR-RED	Jordan (1969)
Renormalized Difference Vegetation Index (RDVI)	$\sqrt{DVI \times NDVI}$	Reujean and Breon (1995)
Optimized Soil Adjusted Vegetation Index (OSAVI)	$\frac{1{,}5 \times NIR - RED}{NIR + RED + 0{,}16}$	Rondeaux et al.. (1996)

Regarding crop yield estimation, literature shows a strong relationship between crop yield and vegetation indices (Anderson et al. 1993; Shanahan et al. 2001; Wiegand and Richardson 1990; Wylie et al. 1991). In most of these studies, a regression relationship was established between vegetation index and observed plant yield, and this relationship was then used to predict crop yields with new vegetation index information. For example, Bolton and Friedl (2013) established a linear regression model between yield and NDVI, EVI, and NDWI indices derived from MODIS satellite data in a study conducted in the Central United States. Tuvdendorj et al. (2019) found that a combination of NDWI, NDVI, and Visible and Shortwave Infrared Drought Index (VSDI) (Zhang et al. 2013) among the nine vegetation indices considered showed the best performance linearly with spring wheat yield.

In most of the studies, instead of using instantaneous satellite observations, the calculated vegetation indices are integrated over a while and correlated with the corresponding crop yield. This is mainly because the relationship between crop yield and spectral reflectance varies with plant growth (Labus et al. 2002). In addition, the temporal integration or aggregation of vegetation indices reduces the noise due to other factors on the vegetation (such as effects from soils and clouds). This leads to a better explanation of the total effect of photosynthesis (Benedetti and Rossini 1993). Aggregation can be performed by taking the maximum value of the vegetation index, averaging the peak values of the vegetation index, summing the vegetation index values in a crop cycle, or taking the vegetation index value during the end of the season.

Funk and Budde (2009) reported that cumulative NDVI from mid- to late-season correlates better with crop yield compared to other methods. Lai et al. (2018) estimated wheat yield as a function of integrated NDVI (obtained during the growing season) calculated from Landsat satellite data with reasonable accuracy in a cereal-growing region in northern Australia. Mirasi et al. (2019) used the sum of NDVI values obtained from Landsat 8 satellite data (during the growing season) as an indicator to estimate wheat yield in Iran. In some studies, a non-linear regression approach was used to predict crop yields using vegetation index values (Holzapfel et al. 2009; Ma et al. 2001; Mkhabela et al. 2011).

In recent years, complex regression and machine learning techniques have also been used to model crop yield and LAI using satellite sensor-based vegetation indices. Some of these techniques include partial least square regression (Li et al. 2014; Nguyen and Lee 2006), artificial neural networks (ANN) (Johnson et al. 2016), support vector machines (Durbha et al. 2007; Tuia et al. 2011), and random forests (Liang et al. 2015).

References

Alahacoon, N., Edirisinghe, M., & Ranagalage, M. (2021). Satellite-based meteorological and agricultural drought monitoring for agricultural sustainability in Sri Lanka. *Sustainability*, *13*(6), 3427.

Anderson, G. L., Hanson, J. D., & Haas, R. H. (1993). Evaluating Landsat Thematic Mapper derived vegetation indices for estimating above-ground biomass on semiarid rangelands. Remote sensing of environment, 45(2), 165-175.

Bastiaanssen, W. G. M. (1998). "Remote sensing in water resources management: The state of the art." International Water Management Institute, Colombo, Sri Lanka.

Benedetti, R., & Rossini, P. (1993). On the use of NDVI profiles as a tool for agricultural statistics: the case study of wheat yield estimate and forecast in Emilia Romagna. Remote Sensing of Environment, 45(3), 311-326.

Bolton, D. K., & Friedl, M. A. (2013). Forecasting crop yield using remotely sensed vegetation indices and crop phenology metrics. Agricultural and forest meteorology, 173, 74-84.

Broge N.H. and Leblanc E. (2001): Comparing prediction power and stability of broadband and hyperspectral vegetation indices for estimation of green leaf area index and canopy chlorophyll density. Remote Sensing of Environment, 76: 156-172.

Chandrasekar, K., Sai, M.V.R.S., Roy, P.S., Dwevedi, R.S. 2010. Land Surface Water Index (LSWI) response to rainfall and NDVI using the MODIS Vegetation Index product. International Journal of Remote Sensing, 31(15), 3987-4005.

Dangwal, N., Patel, N. R., Kumari, M., & Saha, S. K. (2016). Monitoring of water stress in wheat using multispectral indices derived from Landsat-TM. Geocarto International, 31(6), 682-693.

Durbha, S. S., King, R. L., & Younan, N. H. (2007). Support vector machines regression for retrieval of leaf area index from multiangle imaging spectroradiometer. Remote sensing of environment, 107(1-2), 348-361.

Elvanidi, A., Katsoulas, N., Bartzanas, T., Ferentinos, K. P., & Kittas, C. (2017). Crop water status assessment in controlled environment using crop reflectance and temperature measurements. Precision Agriculture, 18, 332-349.

Funk, C., & Budde, M. E. (2009). Phenologically-tuned MODIS NDVI-based production anomaly estimates for Zimbabwe. Remote Sensing of Environment, 113(1), 115-125.

Gao, B.C. 1996. NDWI - A normalized difference water index for remote sensing of vegetation liquid water from space. Remote Sensing of Environment 58: 257-266.

Hama, A., Tanaka, K., Chen, B., & Kondoh, A. (2021). Examination of appropriate observation time and correction of vegetation index for drone-based crop monitoring. *Journal of Agricultural Meteorology*, *77*(3), 200-209.

Hashimoto, N., Saito, Y., Maki, M., & Homma, K. (2019). Simulation of reflectance and vegetation indices for unmanned aerial vehicle (UAV) monitoring of paddy fields. *Remote Sensing*, *11*(18), 2119.

Holzapfel, C. B., Lafond, G. P., Brandt, S. A., Bullock, P. R., Irvine, R. B., Morrison, M. J., ... & James, D. C. (2009). Estimating canola (Brassica napus L.) yield potential using an active optical sensor. Canadian journal of plant science, 89(6), 1149-1160.

Hossain, S. A. A. M., Lixue, W., Taotao, C., & Zhenhua, L. (2017). Leaf area index assessment for tomato and cucumber growing period under different water treatments. *Plant, Soil and Environment*, *63*(10), 461-467.

Huete A.R. (1988): A soil-adjusted vegetation index (SAVI). Remote Sensing of Environment, 25(3): 295-309.

Ihuoma, S. O., & Madramootoo, C. A. (2017). Recent advances in crop water stress detection. Computers and Electronics in Agriculture, 141, 267-275.

Ihuoma, S. O., & Madramootoo, C. A. (2019). Sensitivity of spectral vegetation indices for monitoring water stress in tomato plants. Computers and Electronics in Agriculture, 163, 104860.

Johnson, M. D., Hsieh, W. W., Cannon, A. J., Davidson, A., & Bédard, F. (2016). Crop yield forecasting on the Canadian Prairies by remotely sensed vegetation indices and machine learning methods. Agricultural and forest meteorology, 218, 74-84.

Jordan, C. F. (1969). Derivation of leaf-area index from quality of light on the forest floor. Ecology, 50(4), 663-666.

Jung, M., Henkel, K., Herold, M., & Churkina, G. (2006). Exploiting synergies of global land cover products for carbon cycle modeling. *Remote Sensing of Environment*, *101*(4), 534-553.

Katsoulas, N., Elvanidi, A., Ferentinos, K. P., Kacira, M., Bartzanas, T., & Kittas, C. (2016). Crop reflectance monitoring as a tool for water stress detection in greenhouses: A review. Biosystems Engineering, 151, 374-398.

Knight, J. F., Lunetta, R. S., Ediriwickrema, J., & Khorram, S. (2006). Regional scale land cover characterization using MODIS-NDVI 250 m multi-temporal imagery: A phenology-based approach. *GIScience & Remote Sensing*, *43*(1), 1-23.

Kogan, F. N. (1995). Droughts of the late 1980s in the United States as derived from NOAA polar-orbiting satellite data. Bulletin of the American Meteorological Society, 76(5), 655-668.

Labus, M. P., Nielsen, G. A., Lawrence, R. L., Engel, R., & Long, D. S. (2002). Wheat yield estimates using multi-temporal NDVI satellite imagery. International Journal of Remote Sensing, 23(20), 4169-4180.

Lai, Y., Pringle, M. J., Kopittke, P. M., Menzies, N. W., Orton, T. G., & Dang, Y. P. (2018). An empirical model for prediction of wheat yield, using time-integrated Landsat NDVI. International journal of applied earth observation and geoinformation, 72, 99-108.

Lambin, E. F., Turner, B. L., Geist, H. J., Agbola, S. B., Angelsen, A., Bruce, J. W., ... & Xu, J. (2001). The causes of land-use and land-cover change: moving beyond the myths. *Global environmental change*, *11*(4), 261-269.

Langley, S. K., Cheshire, H. M., and Humes, K. S. (2001). A comparison of single date and multitemporal satellite image classifications in a semi-arid grassland. *Journal of Arid Environments*, *49*(2), 401-411.

Lemenkova, P. (2021). SAGA GIS for computing multispectral vegetation indices by landsat TM for mapping vegetation greenness. *Contemporary Agriculture*, *70*(1-2), 67-75.

Li, X., Zhang, Y., Bao, Y., Luo, J., Jin, X., Xu, X., ... & Yang, G. (2014). Exploring the best hyperspectral features for LAI estimation using partial least squares regression. Remote Sensing, 6(7), 6221-6241.

Liang, L., Di, L., Zhang, L., Deng, M., Qin, Z., Zhao, S., & Lin, H. (2015). Estimation of crop LAI using hyperspectral vegetation indices and a hybrid inversion method. Remote Sensing of Environment, 165, 123-134.

Liu, H.Q. and Huete, A.R. 1995. A feedback based modification of the NDVI to minimize canopy background and atmospheric noise IEEE Transactions on Geoscience and Remote Sensing, 33, pp. 457-465

Ma, B. L., Dwyer, L. M., Costa, C., Cober, E. R., & Morrison, M. J. (2001). Early prediction of soybean yield from canopy reflectance measurements. Agronomy Journal, 93(6), 1227-1234.

Magney, T. S., Vierling, L. A., Eitel, J. U., Huggins, D. R., & Garrity, S. R. (2016). Response of high frequency Photochemical Reflectance Index (PRI) measurements to environmental conditions in wheat. Remote Sensing of Environment, 173, 84-97.

Mirasi, A., Mahmoudi, A., Navid, H., Valizadeh Kamran, K., & Asoodar, M. A. (2021). Evaluation of sum-NDVI values to estimate wheat grain yields using multi-temporal Landsat OLI data. Geocarto International, 36(12), 1309-1324.

Mkhabela, M. S., Bullock, P., Raj, S., Wang, S., & Yang, Y. (2011). Crop yield forecasting on the Canadian Prairies using MODIS NDVI data. Agricultural and Forest Meteorology, 151(3), 385-393.

Nguyen, H. T., & Lee, B. W. (2006). Assessment of rice leaf growth and nitrogen status by hyperspectral canopy reflectance and partial least square regression. European Journal of Agronomy, 24(4), 349-356.

Nordberg, M. L., and Evertson, J. (2005). Vegetation index differencing and linear regression for change detection in a Swedish mountain range using Landsat TM® and ETM+® imagery. *Land Degradation & Development*, *16*(2), 139-149.

Panigada, C., Rossini, M., Meroni, M., Cilia, C., Busetto, L., Amaducci, S., ... & Colombo, R. (2014). Fluorescence, PRI and canopy temperature for water stress detection in cereal crops. International Journal of Applied Earth Observation and Geoinformation, 30, 167-178.

Peng, Y., & Gitelson, A. A. (2011). Application of chlorophyll-related vegetation indices for remote estimation of maize productivity. *Agricultural and Forest Meteorology*, *151*(9), 1267-1276.

Pereira, A. R., Camargo, M. B. P. D., & Villa Nova, N. A. (2011). Coffee crop coefficient for precision irrigation based on leaf area index. *Bragantia*, *70*, 946-951.

Rondeaux, G., Steven, M., & Baret, F. (1996). Optimization of soil-adjusted vegetation indices. Remote sensing of environment, 55(2), 95-107.

Rossini, M., Fava, F., Cogliati, S., Meroni, M., Marchesi, A., Panigada, C., ... & Colombo, R. (2013). Assessing canopy PRI from airborne imagery to map water stress in maize. *ISPRS journal of photogrammetry and remote sensing*, *86*, 168-177.

Roujean, J. L., & Breon, F. M. (1995). Estimating PAR absorbed by vegetation from bidirectional reflectance measurements. Remote sensing of Environment, 51(3), 375-384.

Rouse J.W, Haas R.H., Scheel J.A. & Deering D.W. (1974): Monitoring Vegetation Systems in the Great Plains with ERTS. Proceedings, 3rd Earth Resource Technology Satellite (ERTS) Symposium, 1: 48-62.

Shanahan, J. F., Schepers, J. S., Francis, D. D., Varvel, G. E., Wilhelm, W. W., Tringe, J. M., ... & Major, D. J. (2001). Use of remote-sensing imagery to estimate corn grain yield. Agronomy Journal, 93(3), 583-589.

Shanmugapriya, P., Rathika, S., Ramesh, T., & Janaki, P. (2019). Applications of remote sensing in agriculture-A Review. Int. J. Curr. Microbiol. Appl. Sci, 8(01), 2270-2283.

Tuia, D., Verrelst, J., Alonso, L., Pérez-Cruz, F., & Camps-Valls, G. (2011). Multioutput support vector regression for remote sensing biophysical parameter estimation. IEEE Geoscience and Remote Sensing Letters, 8(4), 804-808.

Tuvdendorj, B., Wu, B., Zeng, H., Batdelger, G., & Nanzad, L. (2019). Determination of appropriate remote sensing indices for spring wheat yield estimation in Mongolia. Remote Sensing, 11(21), 2568.

Wiegand, C. L., & Richardson, A. J. (1990). Use of spectral vegetation indices to infer leaf area, evapotranspiration and yield: I. Rationale. Agronomy Journal, 82(3), 623-629.

Wylie, B. K., Harrington Jr, J. A., Prince, S. D., & Denda, I. (1991). Satellite and ground-based pasture production assessment in Niger: 1986-1988. International Journal of Remote Sensing, 12(6), 1281-1300.

Xiao, X., Zhang, Q., Braswell, B., Urbanski, S., Boles, S., Wofsy, S., ... & Ojima, D. (2004). Modeling gross primary production of temperate deciduous broadleaf forest using satellite images and climate data. *Remote sensing of environment*, *91*(2), 256-270.

Xie, Y., Sha, Z., & Yu, M. (2008). Remote sensing imagery in vegetation mapping: a review. *Journal of plant ecology*, *1*(1), 9-23.

Yan, K., Gao, S., Chi, H., Qi, J., Song, W., Tong, Y., ... & Yan, G. (2021). Evaluation of the vegetation-index-based dimidiate pixel model for fractional vegetation cover estimation. *IEEE Transactions on Geoscience and Remote Sensing*, *60*, 1-14.

Zambrano, F., Lillo-Saavedra, M., Verbist, K., & Lagos, O. (2016). Sixteen years of agricultural drought assessment of the BioBío region in Chile using a 250 m resolution Vegetation Condition Index (VCI). *Remote Sensing*, *8*(6), 530.

Zhang, N., Hong, Y., Qin, Q., & Liu, L. (2013). VSDI: a visible and shortwave infrared drought index for monitoring soil and vegetation moisture based on optical remote sensing. International journal of remote sensing, 34(13), 4585-4609.

6. EVAPOTRANSPIRATION MAPPING BY USING REMOTE SENSING

Atila Bezdan, Jovana Bezdan, Boško Blagojević

The worldwide energy equilibrium considers the movement of energy within Earth's climate system and how it interacts with outer space, as depicted in Figure 6.1. Understanding the various energy movements between the atmosphere and Earth's surface, exceptionally sensible (H) and latent (LE) heat fluxes, and soil moisture levels is crucial for numerous environmental purposes (Liou and Kar, 2014). This includes tracking plant water needs, growth, and yield and being vital for agricultural and irrigation management systems (Kustas et al., 2004; Dodds et al., 2005; Consoli et al., 2006; Liou et al., 1999).

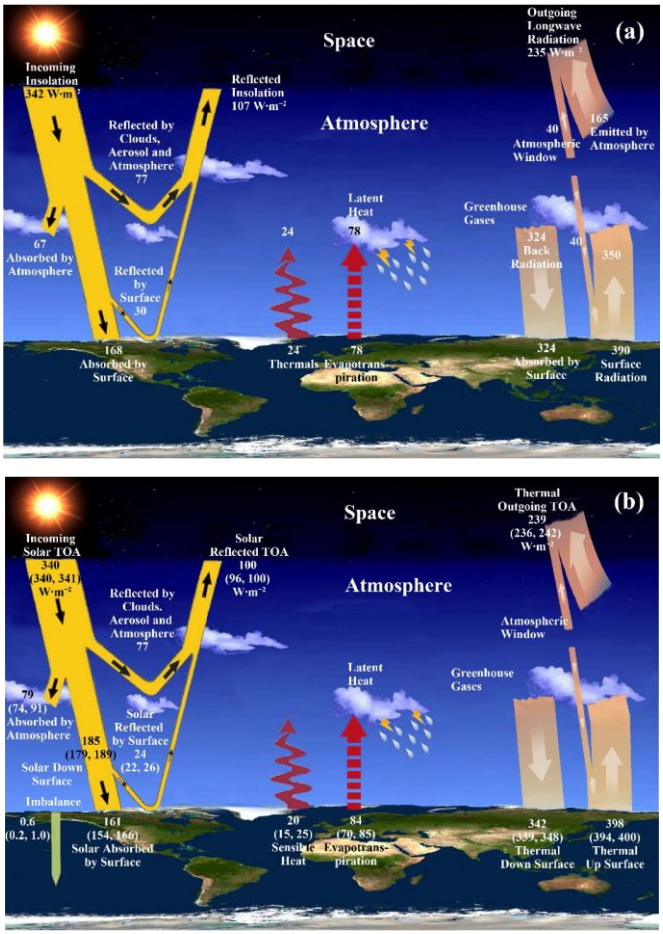

Figure 6.1. Schematic diagram of the Earth's global mean annual energy balance (W·m−2). Numerical values are taken from (a) Kiehl el al. 1997 and (b) Wild et al. 2013.

Evapotranspiration (ET) from land surfaces, encompassing both soil evaporation and plant transpiration to the atmosphere, is a significant process involving substantial water and

heat exchange between the Earth's surface and the lower atmosphere. This process is acknowledged as a crucial element in the hydrological cycle due to its extensive involvement in water and heat transfer (Allen et al., 2007; Long & Singh, 2013). The precise estimation and comprehension of the spatial-temporal variations of ET are essential for numerous applications. These include the development of water balances, monitoring droughts, forecasting crop yields, advancing precision agriculture, and managing water resources effectively (Bastiaanssen et al., 2005; Bastiaanssen & Ali, 2003; Roerink et al., 1997; Ines et al., 2006; Li et al., 2013; Meng et al., 2014; Awan & Ismaeel, 2014; Courault et al., 2005).

Evaporation is the primary mechanism for water removal from a watershed, while transpiration involves water release from plants and other living surfaces with moisture. As such, evapotranspiration, the combination of both evaporation and transpiration, plays a key role in the hydrological cycle. As the most significant water flux exiting Earth's surface, measuring evapotranspiration (ET) is essential for enhancing our understanding of various hydrological, climatic, and ecosystem dynamics. Accurate ET data is also valuable in numerous fields, including water resource management, drought surveillance, improving hydrological models, weather forecasting, and forest fire risk assessment (Anderson et al., 2007; Bastiaanssen et al.,2002).

The ground-based tools for measuring latent (LE) and sensible (H) heat fluxes and soil moisture offer several benefits. However, they typically provide only localized data and can be expensive, time-consuming, labor-intensive, and prone to instrument failure. Combining ground data with remote sensing imagery can frequently offer extensive, repeated insights into critical parameters like land surface interactions and soil moisture. Various methods using diverse remote sensing data have been developed for this. Satellite remote sensing, in particular, has become a prominent tool for gathering spatially detailed information on surface fluxes, thanks to its comprehensive, non-intrusive coverage and ability to overcome accessibility issues. Various algorithms using different remote sensing data types, often combined with other surface and atmospheric data, have been created for parameter estimation. Using satellite data, particularly from optical and thermal infrared radiometers, has proven effective in retrieving LE and H fluxes and soil moisture variations. Thermal infrared data is especially useful for studying biophysical landscape characteristics and ecological modeling. These methods range from empirical to those based on the energy balance equation and the correlation between

satellite-derived vegetation indices and surface radiant temperatures. Recent methodologies include Moran et al. (2004), Courault et al., (2005), and others.

Evapotranspiration (ET), encompassing both transpiration and evaporation, is a critical hydrological flux that is challenging to estimate, especially at larger scales. Traditional ET estimation methods, like lysimeters, eddy covariance, and others, are effective locally but struggle with large-scale applications due to land surface heterogeneity and complex hydrological processes. Remote sensing offers a promising alternative for mapping ET patterns at regional to mesoscale, using data from visible, near-infrared, and thermal infrared bands to retrieve critical surface and atmospheric variables. This technology provides broad coverage at a lower cost than conventional methods and is the only viable option for areas without ground measurements. Remotely sensed surface temperature data, varying in resolution, helps link surface radiances to energy balance components.

6.1. Surface Energy Balance Models

- Surface Energy Balance

The surface energy balance at the land-air interface can be written as Equation (1) as follows, and the net radiation is considered as a residual of the soil heat flux, the sensible heat flux, and the latent heat flux:

$$Rn = G + H + LE \quad (1)$$

where G is the soil heat flux ($W \cdot m^{-2}$), H is the sensible heat flux ($W \cdot m^{-2}$), and LE is the latent heat flux ($W \cdot m^{-2}$). Net radiation (Rn) is partitioned into G, H, and LE. It can be estimated from the sum of the difference between the incoming ($Rs\downarrow$) and the reflected outgoing shortwave solar radiation ($Rs\uparrow$) (0.15 to 5 μm), and the difference between the downwelling atmospheric ($RL\downarrow$) and the surface-emitted and -reflected longwave radiation ($RL\uparrow$).

***- Net Radiation* (*Rn*)**

According to the radiation balance, the net radiation can be considered as a balance between incoming and outgoing short-wave and long-wave radiation under steady atmospheric conditions:

$$R = R\downarrow + R\uparrow + R\downarrow - R\uparrow \quad (2)$$

where *Rn* is the net radiation ($W \cdot m^{-2}$), *Rs*↓ is the incoming short-wave radiation ($W \cdot m^{-2}$), and *Rs*↑ is the outgoing short-wave radiation ($W \cdot m^{-2}$), while *RL*↓ is the incoming long-wave radiation ($W \cdot m^{-2}$), and *RL*↑ is the outgoing long-wave radiation ($W \cdot m^{-2}$). The net short-wave radiation can be written as follows:

$$\sum R_s = (1-\alpha) R_s \downarrow = (1-\alpha) \cdot (S_c \times \cos\theta \times d_r \times \tau_a) \quad (3)$$

where α is the surface albedo, *Sc* is the solar constant ($W \cdot m^{-2}$), θ is the solar incidence angle, *dr* is the relative Earth-Sun distance, and τa is the atmospheric transmissivity.

The incoming long-wave radiation is the downward thermal radiation flux from the atmosphere. The air emissivity can be estimated by a function of the water vapor, pressure, and temperature in the cloudless atmosphere:

$$R_L \downarrow = e_{sky} \times \sigma \times T_a^4 \quad (4)$$

where *esky* is the air emissivity, σ is the Stefan-Boltzmann constant ($W \cdot m^{-2} \cdot K^{-4}$), and *Ta* is the air temperature (K). The outgoing long-wave radiation is computed by using the Stefan-Boltzmann equation:

$$R_L \uparrow = \varepsilon_0 \times \sigma \times T_s^4 \quad (5)$$

where ε_0 is the surface emissivity and *Ts* is the surface temperature (K).

- *Sensible Heat Flux* (*H*)

The sensible heat flux (*H*) is the rate of heat loss to the air by convection and conduction due to a temperature difference, which can be written as:

$$H = \rho_{air} C_p \frac{dT}{r_{ah}} \quad (6)$$

where ρ_{air} is the density of air ($kg \cdot m^{-3}$), *Cp* is the air specific heat (1004 $J \cdot kg^{-1} \cdot K^{-1}$), while *dT* is the difference between the air temperature and the aerodynamic temperature near the surface, ($dT = Ta - Ts$), calculated as set out in the SEBAL Users Manual (Waters et al., 2002) and *rah* is the erodynamic resistance.

- *Latent Heat Flux* (*LE*)

Latent heat flux is the rate of latent heat loss from the surface due to evapotranspiration. According to the Equation (1), the latent heat can be written as:

$$LE = Rn - G - H \quad (7)$$

6.2. Different Surface Energy Balance Algorithms

A large number of remote sensing-based ET models rely on energy balance theory. Gowda et al. (2007) comprehensively reviewed these existing models based on energy balance. They discussed and compared a variety of ET models, including the Surface Energy Balance Index (SEBI) by Meneti and Choudhary (1993), the Surface Energy Balance System (SEBS) by Su (2002), the Simplified Surface Energy Balance Index (S-SEBI) by Roerink et al. (2000), the Two-Source Energy Balance model (TSEB) by Anderson et al. (1997), and the Surface Energy Balance Algorithm for Land (SEBAL) by Bastiaanssen et al. (1998). Additionally, they reviewed SEBAL-like ET estimation models such as the Satellite-based energy balance for mapping evapotranspiration with internalized calibration (METRIC) by Allen et al. (2007), TSEBAL by Wang et al. (2014), and M-SEBAL by Long and Singh (2012).

- *Surface Energy Balance Index* (*SEBI*)

Drawing from the differences between arid and humid areas, Menenti and Choudhury developed the Surface Energy Balance Index (SEBI) method, as outlined in their 1993 study (Choudhury and Menenti, 1993). This approach is used to calculate evapotranspiration based on the evaporative fraction and is inspired by the Crop Water Stress Index (CWSI) concept, introduced by Van den Hurk in 2001. The SEBI method operates by adjusting the measured surface temperature within a defined maximum range. This range is established by the extreme values in the surface energy balance, which represent theoretical minimum and maximum differences between surface and air temperatures.

- *Surface Energy Balance System* (*SEBS*)

The Surface Energy Balance System (SEBS) is another prominent model in the field. In various studies (Su et al. 2001, 2002) and Su et al. (2003, 2005), Su detailed a revised version of the SEBI method, now known as SEBS. This model is specifically designed for calculating land surface energy balance using data from remote sensing and standard meteorological sources. SEBS primarily focuses on estimating sensible and latent heat fluxes through satellite data. Its core methodology includes computation of land surface physical parameters, determining roughness length for heat transfer, and calculating the evaporative fraction, all

based on the energy balance under limiting conditions, as proposed initially by Choudhury in 1989.

- *Simplified Surface Energy Balance Index* (*S-SEBI*)

Roerink et al. 2000 introduced a new, more straightforward approach derived from the SEBI model, the Simplified Surface Energy Balance Index (S-SEBI). This method is designed for estimating surface fluxes using remote sensing data. S-SEBI primarily relies on the contrast between maximum and minimum surface temperatures, dependent on surface reflectance (albedo) under dry and wet conditions, respectively. This contrast is crucial for dividing the available energy into sensible and latent heat fluxes. One of the critical advantages of S-SEBI is that it doesn't require additional meteorological data if the surface temperature extremes for the area under study are known. The method assumes constant global radiation and air temperature, allowing for a physical interpretation of the observed surface reflectance and temperature variations within an image, particularly in scenarios where surface characteristics vary between dark/wet and dry/bright pixels.

- *Surface Energy Balance Algorithm for Land* (*SEBAL*)

The Surface Energy Balance Algorithm for Land (SEBAL) is an image-processing model aimed at calculating evapotranspiration (ET) as a residual of the surface energy balance. It was developed in the Netherlands by Bastiaanssen et al., as detailed in their studies from 1998a and 1998b. SEBAL is recognized as one of the most promising methods for estimating evapotranspiration at local and regional scales, requiring minimal ground data. It represents an intermediate approach that combines empirical relationships with physical parameterizations.

The model utilizes digital satellite imagery data capable of measuring visible, near-infrared, and thermal infrared radiation alongside Ts, NDVI, and albedo maps. It estimates latent heat flux (LE) as a residual of the energy balance equation on a pixel-by-pixel basis. Net radiation (Rn) is derived from the balance of short and longwave radiation, and soil heat flux (G) is calculated using an equation by Bastiaanssen, which is adaptable to various types of vegetation cover and soil.

SEBAL's effectiveness has been confirmed under various climatic conditions, both at field and catchment scales. It has demonstrated typical accuracies of 85% at the field scale and

95% on daily and seasonal scales, respectively, as per the findings in Bastiaanssen et al., 1998b and 2005, with successful applications in over 30 countries globally.

- *Mapping Evapotranspiration at High Resolution and with Internalized Calibration* (*METRIC*)

Mapping Evapotranspiration at High Resolution with Internalized Calibration (METRIC) is a modification of the SEBAL energy balance model, initially developed in the Netherlands. METRIC is an image-processing tool designed for mapping regional evapotranspiration (ET) over complex surfaces by calculating the residual energy balance at the Earth's surface. This model expands on SEBAL by incorporating reference ET, which is calculated using terrestrial weather data.

The core concept of METRIC, as highlighted by Allen et al. in their 2005 and 2007 studies, is that evaporation, involving liquid drops absorbing heat, can be tracked using remotely sensed data in the visible, near-infrared, and thermal infrared spectra. This is combined with ground-based wind speed measurements and near-surface dew point temperature. METRIC employs two "anchor conditions" within a given scene for internal calibration. This calibration simplifies the computation of sensible and latent heat fluxes and sets the boundaries for the energy balance.

This internal calibration process, akin to that in SEBAL, minimizes the need for atmospheric correction of surface temperature or reflectance measurements, as outlined by Tasumi et al. in 2005. It also reduces potential biases in estimating aerodynamic stability correction or surface roughness. Calibration involves manually selecting a hot and a cold pixel to establish the range of vertical temperature gradients above the surface. The "cold" condition typically represents a well-irrigated alfalfa field where ET equals the reference ET for standardized 0.5 m tall alfalfa, while the "hot" condition is often a dry, bare agricultural field where ET is zero.

- *Two-Source Models* (*TSM*)

Norman and Becker introduced a novel approach in 1995, known as the two-source model, also called the dual-source model, to enhance the accuracy of latent heat (LE) estimations from satellite remote sensing data, particularly over sparsely vegetated areas. This development is detailed in their work (Norman and Becker, 1995) as well as in related studies by Blyth and

Harding (1995), Huntingford et al. (1995), Kabat et al. (1997), Wallace (1997), and Priestley and Taylor (1972).

The fundamental concept of this model involves separating the composite radiometric surface temperature into two distinct components: soil and vegetation. It then accounts for the sensible and latent heat fluxes transferred to the atmosphere from both surface elements. A vital advantage of the dual-source model is its independence from ground-based information or any prior calibration. This aspect significantly broadens its applicability, allowing for accurate estimations without additional input data.

6.3. Example: Surface energy balance using the METRIC model and water R package

In the following text we describe the application of the METRIC model for calculating the surface energy balance using the Water *R* package. The following material was developed by Guillermo Federico Olmedo and Daniel de la Fuente-Saiz (http://cran.nexr.com/web/packages/water/). This example presents the procedure to estimate the Land Surface Energy Balance (LSEB) using lansat imagery and the Water *R* package. It follows the METRIC model methodology (Allen et al., 2007) to estimate the LSEB using Landsat 7 and 8 satellite images. The Water *R* package can be found at:

http://cran.nexr.com/web/packages/water/

https://github.com/midraed/water

General Aproach

One of the most cited models to estimate land surface evapotranspiration from satellite-based energy balance is the Mapping of EvapoTranspiration at high Resolution with Internalized Calibration (METRIC). This model was developed by Allen et al., (2007) based on the well-known SEBAL model (Bastiaanssen, 1998). Satellite images have been widely applied in many countries worldwide to estimate crop evapotranspiration (ET) at field scales and over large areas. The model has been used in different vegetation and crop types such as wheat, corn, soybean, and alfalfa with good results (3 - 20% error) and also in recent years over sparse woody

canopies such as vineyards and olive orchards, in both plain and mountainous terrain. Thus, ET is estimated as a residual of the surface energy equation:

$LE = Rn - G - H$

where LE is latent energy consumed by ET; Rn is net radiation; G is sensible heat flux conducted into the ground; and H is sensible heat flux convected to the air.

Rn, G , and H are estimated for each pixel into a *Landsat satellite scene*, supported by one weather station. Then LE is estimated by fluxes using the previous equation, and after that, the instantaneous evapotranspiration values are as:

$$ET_{inst} = 3600 \cdot \frac{LE}{\lambda \rho_{\varpi}}$$

where ET_{inst} is the instantaneous ET at the satellite flyby; 3600 is the converting factor from seconds to hours; ρ_w is the density of water = 1000 kg·m^{-3}; and λ is the water latent heat of vaporization.

Finally, the daily ET is computed pixel by pixel (30 x 30 m) as:

$$ET_{24} = \frac{ET_{inst}}{ET_r} \cdot ET_{r\_24}$$

First, the WATER package must be loaded to begin this procedure:

```
library(water)
```

Base data preparation

The water package and a simple procedure were used to calculate crop Evapotranspiration based on the METRIC approach. Three sources are as follows:

- A raw Landsat 7/8 satellite image (original .TIF data from USGS).
- A Weather Station data (.CSV file).
- A polygon with our Area-of-interest (AOI) Spatial-Polygon object (if we won`t estimate corp ET for the entire Landsat scene).

In this example, the ET will be calculated for the selected area located in North Serbia, near one of the main meteorological stations in this region, weather station Rimski Sancevi, and the Landsat 8 satellite images for July 11, 2023, will be used.

As a first step, the AOI polygon should be created by using bottom right and top left points:

```
aoi <- createAoi(topleft = c(404741, 5048480),
                 bottomright = c( 426281, 5030240), EPSG = 32634)
```

Then the working directory where files should be located is set:

```
setwd("D:/data")
```

Then, the weather station data should be loaded. For that, we are going to use the function called read.WSdata. This function converts the .csv file into a waterWeatherStation object. Then, if we provide a Landsat metadata file (.MTL file), we can calculate the time-specific weather conditions at the time of satellite overpass.

```
csvfile <- "RimskiSancevi.csv"
MTLfile <- "L8.MTL.txt"
WeatherStation <- read.WSdata(WSdata = csvfile,
                              datetime.format =  "%Y/%m/%d %H:%M",
                        columns=c("date" = 1, "time" = 1,
                        "radiation" = 5, "wind" = 6, "RH" = 3,
                        "temp" = 2, "rain" = 4), lat=45.50,
                        long= 19.91, elev=78, height= 2.0,
                        tz="Europe/Belgrade",  MTL = MTLfile)
```

We can visualize the weather station data as (Figure 6.2):

```
plot(WeatherStation, alldata=FALSE)
```

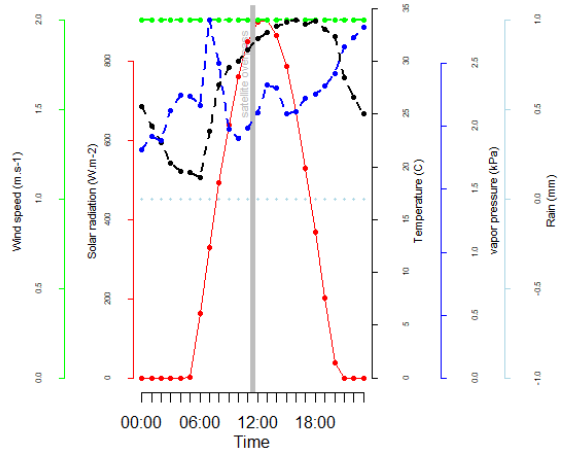

Figure 6.2 Graph of the weather station data

To be able to run METRIC with Landsat 8 data, the ESPA surface reflectance products must be available in the working directory. The Landsat scene can loaded using *loadImage()* function. And the SR data with *loadImage.SR*:

```
image.DN <- loadImage(path=getwd(), aoi=aoi, sat="L8")
image.SR <- loadImageSR(path=getwd(), aoi=aoi)
```

The satellite images can be visualized as (Figure 6.3 and 6.4):

```
plot(image.DN)
```

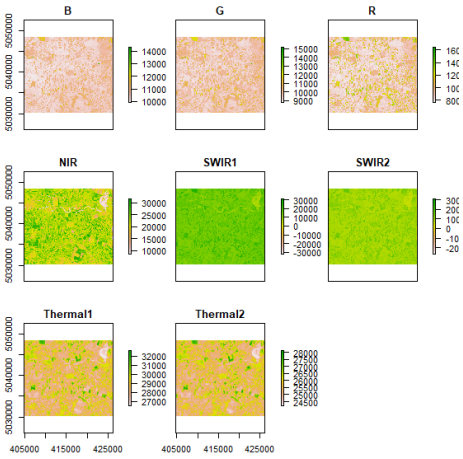

Figure 6.3 Landsat 8 images

```
plot(image.SR)
```

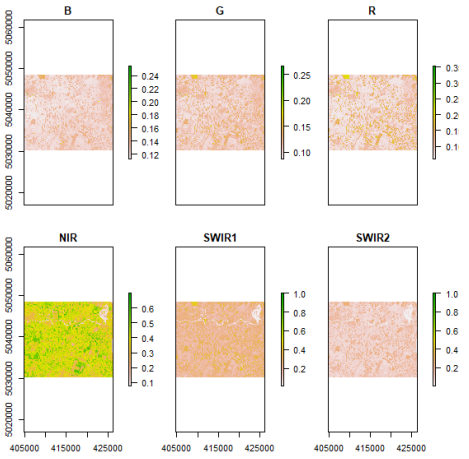

Figure 6.4 Landsat 8 images (Surface Reflectance)

Surface Energy Balance estimation

We are going to use the function called METRIC.EB will estimate the land surface energy balance. This function has many parameters to choose from the different METRIC model equations. e.g., you can change:

- Coefficients used to estimate broadband albedo.
- Model to estimate Leaf Area Index (LAI) from satellite data.
- Model to estimate momentum roughness length (Zom)
- Automatic method to select anchor pixels
- ETr coefficient and momentum roughness length for the weather station

When we run METRIC.EB, the energy balance, and the surface temperature (Ts) are assigned to the Energy Balance object. Also, the function prints the position and some other data from the anchor pixels (Figure 6.5) and finally plots the values of the aerodynamic resistance during the iterative process.

```
Energy.Balance <- METRIC.EB(image.DN = image.DN, image.SR = image.SR,
                            plain=TRUE, aoi=aoi, n = 5,
                            WeatherStation = WeatherStation,
                            anchors.method = "best",
```

```
                ETp.coef = 1.2, sat="L8",
                alb.coeff = "Olmedo", LST.method = "SW",
                LAI.method = "metric2010", Z.om.ws = 0.03,
                MTL = MTLfile)
```

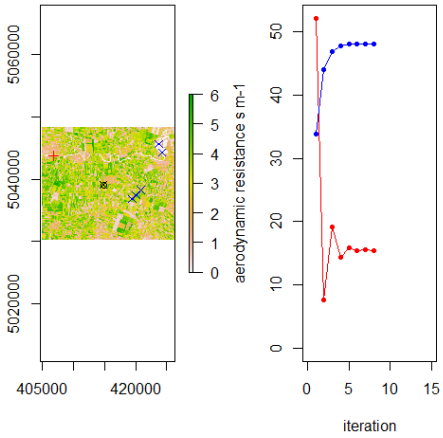

Figure 6.5 LAI and hot and cold pixels (iterative process)

Then the energy balance components can be visualized as (Figure 6.6):

```
plot(Energy.Balance$EB)
```

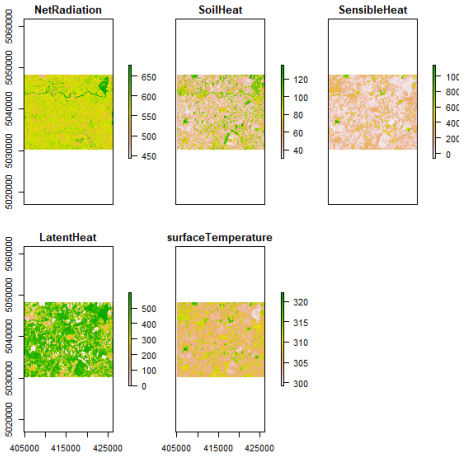

Figure 6.6 Components of the energy balance

Daily Crop Evapotranspiration (ET_24) estimation

To estimate the daily crop evapotranspiration from the Landsat scene, we need the daily reference ET (ETr) for our weather station so that we can calculate the daily ETr with:

```
ET_WS <- dailyET(WeatherStation = WeatherStation, MTL = MTLfile)
```

And finally, we can estimate daily crop ET pixel by pixel (Figure 6.7):

```
ET.24 <- ET24h(Rn=Energy.Balance$EB$NetRadiation,
               G=Energy.Balance$EB$SoilHeat,
               H=Energy.Balance$EB$SensibleHeat,
               Ts=Energy.Balance$EB$surfaceTemperature,
               WeatherStation = WeatherStation, ETr.daily=ET_WS)
```

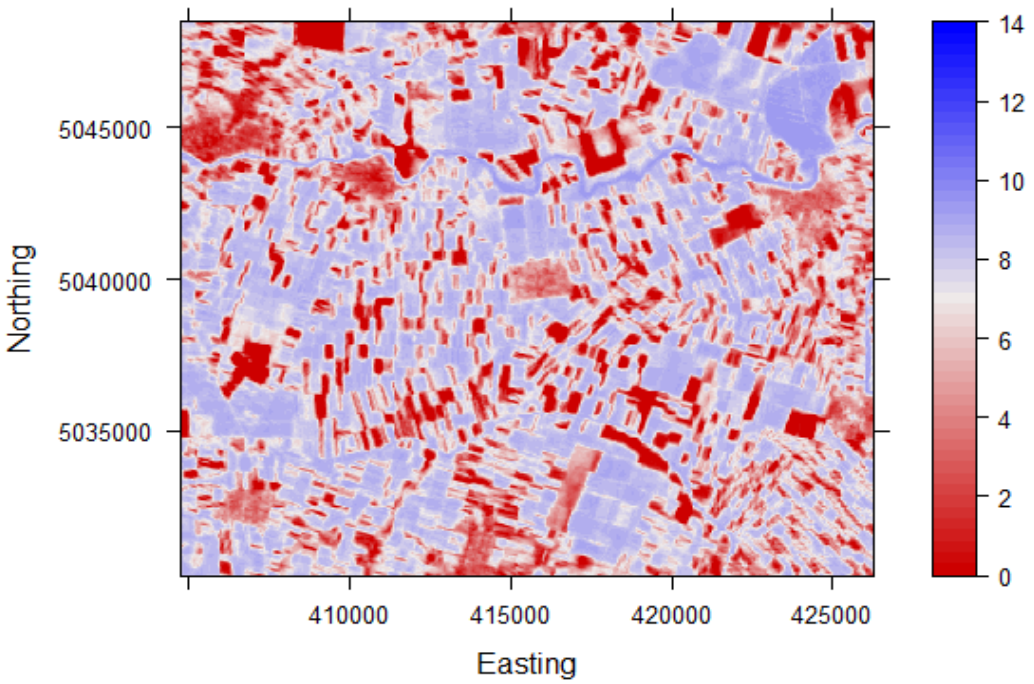

Figure 6.7 Daily crop evapotranspiration (mm/day)

The final result can be exported as a TIFF file and opened in GIS software for further analysis (Figure 6.8):

```
writeRaster(ET.24, filename="ET.tif", format="GTiff", overwrite=TRUE)
```

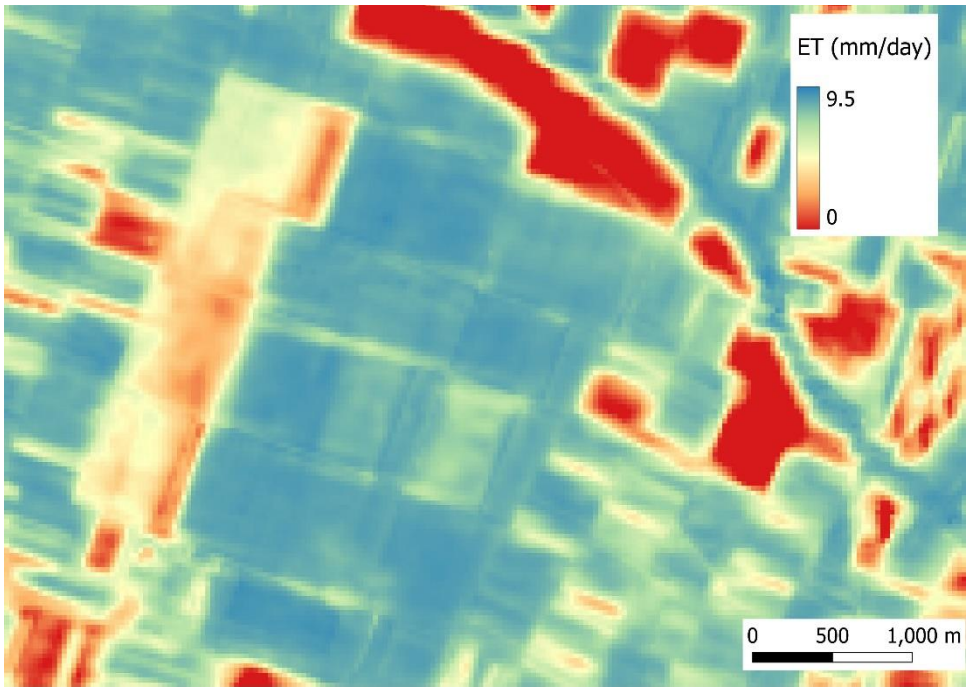

Figure 6.8 Map of the daily crop evapotranspiration in GIS software

References

Allen, R. G., M. Tasumi & R. Trezza (2007). Satellite-based energy balance for mapping evapotranspiration with internalized calibration (METRIC) - Model. Journal of Irrigation and Drainage Engineering-Asce, 133, 380-394.

Allen, R.G.; Tasumi, M.; Morse, A. (2005). Satellite-based evapotranspiration by METRIC and Landsat for western states water management. Presented at the US Bureau of Reclamation Evapotranspiration Workshop, Ft. Collins, CO, USA, 8–10 February 2005.

Allen, R.G.; Tasumi, M.; Trezza, R. *(*2007). Satellite-based energy balance for mapping evapotranspiration with internalized calibration (METRIC)-model. *J. Irrig. Drain. E ASCE 133*, 380–394.

Anderson, M., J. Norman, G. Diak, W. Kustas & J. Mecikalski (1997). A two-source time integrated model for estimating surface fluxes using thermal infrared remote sensing. Remote sensing of environment, 60, 195-216.

Anderson, M.C.; Norman, J.M.; Mecikalski, J.R.; Otkin, J.A.; Kustas, W.P. (2007). A climatological study of evapotranspiration and moisture stress across the continental

United States based on thermal remote sensing: 1. Model formulation. *J. Geophys. Res. Atmos.*, *112*, D10117.

Awan, U. K. & A. Ismaeel (2014). A new technique to map groundwater recharge in irrigated areas using a SWAT model under changing climate. Journal of Hydrology, 519, 1368-1382.

Bastiaanssen, W. G. M. & S. Ali (2003). A new crop yield forecasting model based on satellite measurements applied across the Indus Basin, Pakistan. Agriculture Ecosystems & Environment, 94, 321-340.

Bastiaanssen, W. G. M., E. J. M. Noordman, H. Pelgrum, G. Davids, B. P. Thoreson & R. G. Allen (2005). SEBAL model with remotely sensed data to improve water-resources management under actual field conditions. Journal of Irrigation and Drainage Engineering-Asce, 131, 85-93.

Bastiaanssen, W. G. M., M. Menenti, R. A. Feddes & A. A. M. Holtslag (1998). A remote sensing surface energy balance algorithm for land (SEBAL) - 1. Formulation. Journal of Hydrology, 212, 198-212.

Bastiaanssen, W.G.M. (2000). SEBAL-based sensible and latent heat fluxes in the irrigated Gediz Basin, Turkey. *J. Hydrol.*, *229*, 87–100.

Bastiaanssen, W.G.M.; Ahmad, M.U.D.; (2002). Chemin, Y. Satellite surveillance of evaporative depletion across the Indus Basin. *Water Resour. Res.*, *38*, 1273.

Bastiaanssen, W.G.M.; Pelgrum, H.; Wang, J.; Ma, Y.; Moreno, J.F.; Roerink, G.J.; van der Wal, T. (1998). A remote sensing surface energy balance algorithm for land (SEBAL): 2. Validation. *J. Hydrol. 212–213*, 213–229.

Blyth, E.M.; Harding, R.J (1995). Application of aggregation models to surface heat flux from the Sahelian tiger bush. *Agric. For. Meteorol.*, *72*, 213–235.

Choudhury, B.J. (1989). Estimating evaporation and carbon assimilation using infrared temperature data: vistas in modeling. In *Theory and Applications of Optical Remote Sensing*; Asrar, G., Ed.; Wiley: New York, NY, USA,; pp. 628–690.

Choudhury, B.J.; Menenti, M. (1993). *Parameterization of Land Surface Evaporation by means of Location Dependent Potential Evaporation and Surface Temperature Range*; Department for Environment, Food and Rural Affairs (Defra): London, UK,; Volume 212, pp. 561–568.

Consoli, S.; Urso, G.; Toscano, A. Remote sensing to estimate ET-fluxes and the performance of an irrigation district in southern Italy. *Agric. Water Manag.* 2006, *81*, 295–314.

Courault, D., B. Seguin & A. Olioso (2005). Review on estimation of evapotranspiration from remote sensing data: From empirical to numerical modeling approaches. Irrigation and Drainage Systems, 19, 223-249.

De Troch, F.P.; Troch, P.A.; Su, Z.; Lin, D.S. (1996). Application of remote sensing for hydrological modelling. In Distributed Hydrological Modeling; Abbott, M.B., Refsgaard, J.C., Eds.; Dordrecht: Kluwer, The Netherlands, pp. 165–191

Dodds, P.E.; Meyer, W.S.; Barton, A. (2005). *A Review of Methods to Estimate Irrigated Reference Crop Evapotranspiration across Australia*; Document prepared for Irrigation Features Technical Report, Australia,

Engman, E.T.; Gurney, R.J. (1991). *Remote Sensing in Hydrology*; Chapman and Hall: London, UK.

Engman, E.T.; Schultz, G.A. (2004). Future perspectives. In *Remote Sensing in Hydrology and Water Management*; Schultz, G.A., Engman, E.T., Eds.; Springer: Berlin, Germany, 2000; pp. 445–457. *Environ.*, *92*, 535–547.

Gowda, P., J. Chavez, P. Colaizzi, S. Evett, T. Howell & J. Tolk (2007). Remote sensing based energy balance algorithms for mapping ET: Current status and future challenges. Transactions of the ASABE, 50, 1639-1644.

Hatfield, J.L. (1983). Evapotranspiration Obtained from Remote Sensing Methods. *Adv. Irrig.*, *2*, 395–416.

Huntingford, C.; Allen, S.; Harding, R. (1995). An intercomparison of single and dual-source vegetation-atmosphere transfer models applied to transpiration from Sahelian savannah. *Bound Lay. Meteorol.*, *74*, 397–418

Idso, S.B.; Jackson, R.D.; Reginato, R.J. (1975). Detection of soil moisture by remote surveillance. *Amer. Sci.*, *63*, 549–557.

Idso, S.B.; Jackson, R.D.; Reginato, R.J. (1975b). Estimating evaporation: A technique adaptable to remote sensing. *Science*, *189*, 991–992.

Ines, A. V. M., K. Honda, A. Das Gupta, P. Droogers & R. S. Clemente (2006). Combining remote sensing-simulation modeling and genetic algorithm optimization to explore water management options in irrigated agriculture. Agricultural Water Management, 83, 221- 232.

Kabat, P.; Dolman, A.J.; Elbers, J.A. (1997). Evaporation, sensible heat and canopy conductance of fallow savannah and patterned woodland in the Sahel. *J. Hydrol.*, *188–189*, 494–515.

Kiehl, J.T.; Trenberth, K.E. (1997). Earth's annual global mean energy budget. *Bull. Am. Meteorol. Soc.*, *78*, 197–208.

Kustas, W.P.; Jackson, T.J.; Prueger, J.H.; MacPherson, J.I.; Wolde, M. (2004). Effects of remote sensing pixel resolution on modelled energy flux variability of croplands in Iowa. *Remote Sens. Environ.*, *92*, 535–547.

Kustas, W.P.; Norman, J.M. (1996). Use of remote sensing for evapotranspiration monitoring over land surfaces. *Hydrol. Sci. J.*, *41*, 495–516.

Li, Z. Y., X. H. Liu, T. X. Ma, D. Kejia, Q. P. Zhou, B. Q. Yao & T. L. Niu (2013). Retrieval of the surface evapotranspiration patterns in the alpine grassland-wetland ecosystem applying SEBAL model in the source region of the Yellow River, China. Ecological Modelling, 270, 64-75.

Liou, Y.A. and Kar, S.K., (2014). Evapotranspiration estimation with remote sensing and various surface energy balance algorithms—A review. *Energies*, *7*(5), pp.2821-2849.

Liou, Y.-A.; England, A.W. (1996). Annual temperature and radio brightness signatures for bare soils. *IEEE Trans. Geosci. Remote Sens.*, *34*, 981–990.

Liou, Y.-A.; Galantowicz, J.; England, A.W. (1999). A land surface process radio brightness with coupled heat and moisture transport for prairie grassland. *IEEE Trans. Geosci. Remote Sens.*, *37*, 1848–1859.

Liou, Y.-A.; Tzeng, Y.-C.; Wigneron, J.-P. (2002). Probing soil moisture profiles by microwave radiometry over a wheat field. In *Remote Sensing and Hydrology*; Owe, M., Brubaker, K., Eds.; IAHS Redbook Publications: Wallingford, UK,; Volume 267.

Long, D. & V. P. Singh (2012). A modified surface energy balance algorithm for land (MSEBAL) based on a trapezoidal framework. Water Resources Research, 48.

Long, D. & V. P. Singh (2013). Assessing the impact of end- member selection on the accuracy of satellite- based spatial variability models for actual evapotranspiration estimation. Water Resources Research, 49, 2601-2618.

Long, D.; Singh, V.P.; Scanlon, B.R. (2012). Deriving theoretical boundaries to address scale dependencies of triangle models for evapotranspiration estimation. *J. Geophys. Res. Atmos.*, *117*, D05113.

Meneti, M. & B. Choudhary (1993). Parameterization of land surface evapotranspiration using a location dependent potential evapotranspiration and surface temperature range. Exchange Processes at the land Surface for a Range of Space and time series, Bolle, HJ, Feddes, RA,

and Kalma, JD. International Association of Hydrological Sciences Publication, 212, 561-568.

Meng, L., D. Long, S. M. Quiring & Y. J. Shen (2014). Statistical analysis of the relationship between spring soil moisture and summer precipitation in East China. International Journal of Climatology, 34, 1511-1523.

Moran, M.S.; Peters-Lidard, C.D.; Watts, J.M.; McElroy, S. (2004). Estimating soil moisture at the watershed scale with satellite-based radar and land surface models. *Can. J. Remote Sens.*, *30*, 805–824.

Norman, J.M.; Becker, F. (1995). Terminology in thermal infrared remote sensing of natural surfaces. *Agric. For. Meteorol*., *77*, 153–166.

Priestley, C.H.B.; Taylor, R.J. On the assessment of surface heat flux and evaporation using large-scale parameters. *Mon. Weather Rev*. 1972, *100*, 81–92.

Quattrochi, D.A.; Luvall, J.C. (1999). Thermal infrared remote sensing for analysis of landscape ecological processes: Methods and applications. *Landsc. Ecol*., *14*, 577–598.

Rango, A. Application of remote sensing methods to hydrology and water resources. *Hydrol. Sci.J*. 1994, *39*, 309–320.

Roerink, G. J., W. G. M. Bastiaanssen, J. Chambouleyron & M. Menenti (1997). Relating Crop Water Consumption to Irrigation Water Supply by Remote Sensing. Water Resources Management, 11, 445-465.

Roerink, G. J., Z. Su & M. Menenti (2000). S-SEBI: A simple remote sensing algorithm to estimate the surface energy balance. Physics and Chemistry of the Earth, Part B: Hydrology, Oceans and Atmosphere, 25, 147-157.

Roerink, G.J.; Su, Z.; Menenti, M. (2000). S-SEBI: A simple remote sensing algorithm to estimate the surface energy balance. *Phys. Chem. Earth B*, *25*, 147–157.

Sandholt, I.; Rasmussen, K.; Andersen, J. A (2002). Simple interpretation of the surface temperature/ vegetation index space for assessment of soil moisture status. *Remote Sens. Environ.*, *79*, 213–224.

Stisen, S.; Sandholt, I.; Norgaard, A.; Fensholt, R.; Jensen, K.H. (2008). Combining the triangle method with thermal inertia to estimate regional evapotranspiration—Applied to MSG SEVIRI data in the Senegal River basin. *Remote Sens. Environ.*, *112*, 1242–1255.

Su, Z. (2002). The Surface Energy Balance System (SEBS) for estimation of turbulent heat fluxes. Hydrology and Earth System Sciences Discussions, 6, 85-100.

Su, Z. (2001). A Surface Energy Balance System (SEBS) for estimation of turbulent heat fluxes from point to continental scale. In *Advanced Earth Observation—Land Surface Climate*; Su, Z., Jacobs, J., Eds.; Publications of the National Remote Sensing Board (BCRS): Delft, The Netherlands, Volume 01–02, pp. 91–108.

Su, Z. (2005). Hydrological applications of remote sensing. Surface fluxes and other derived variables surface energy balance. In *Encyclopedia of Hydrological Sciences*; Anderson, M., Ed.; John Wiley and Sons: Hoboken, NJ, USA.

Su, Z. (2002). The surface energy balance system (SEBS) for estimation of turbulent heat fluxes. *Hydrol. Earth Syst. Sci.*, *6*, 85–99.

Su, Z.; Li, X.; Zhou, Y.; Wan, L.; Wen, J.; Sintonen, K. (2003). Estimating areal evaporation from remote sensing. *Proc. IEEE Int.*, *2*, 1166–1168.

Tasumi, M.; Trezza, R.; Allen, R.G.; Wright, J.L. (2005). Operational aspects of satellite-based energy balance models for irrigated crops in the semi-arid U.S. *Irrig. Drain. Sys.*, *19*, 355–376.

Van den Hurk, B. (2001). Energy balance based surface flux estimation from satellite data, and its application for surface moisture assimilation. *Meteorol. Atmos. Phys.*, *76*, 43–52.

Wallace, J.S. Evaporation and radiation interception by neighbouring plants. *Q. J. R. Meteorol.Soc*. 1997, *123*, 1885–1905.

Wang, X. G., W. Wang, D. Huang, B. Yong & X. Chen (2014). Modifying SEBAL Model Based on the Trapezoidal Relationship between Land Surface Temperature and Vegetation Index for Actual Evapotranspiration Estimation. Remote Sensing, 6, 5909-5937.

Waters, R.; Allen, R.; Tasumi, M.; Trezza, R.; Bastiaanssen, W. (2002). *SEBAL. Surface Energy Balance Algorithms for Land*, Version 1.0; Idaho Implementation, Advance Training and Users Manual; August 2002.

Wild, M.; Folini, D.; Schar, C.; Loeb, N.; Dutton, E.G.; Langlo, G.K. (2013).The global energy balance from a surface perspective. *Clim. Dyn.*, *40*, 3107–3134.

7. Unmanned Aerial Vehicle (UAV) Systems for Irrigation Management

Dr. Emre Tunca Dr. Eyüp Selim Köksal

Integrating Unmanned Aerial Vehicles (UAVs) into irrigation management represents a substantial advancement in agricultural technology, offering promising solutions to optimize irrigation water management in farming. This part explores the current state and future potential of UAV systems in irrigation management, focusing on applying Evapotranspiration (ET) estimation models and their implications for sustainable agriculture.

UAVs have increasingly become a tool of choice for precision irrigation management, providing high-resolution data vital for efficient water resource allocation. This precision is crucial in global water scarcity and the increasing need for sustainable agricultural practices. Research by Tunca (2023) and Cheng et al. (2022) highlights how UAVs, equipped with multispectral and thermal sensors, can effectively monitor crop water stress and soil moisture levels, providing essential data for irrigation scheduling.

A combination of UAVs and ET estimation models has revolutionized irrigation practices. ET estimation models, such as the Modified Penman-Monteith method, FAO-56, and others, have been traditionally used for irrigation planning (Zhang et al., 2023). However, their integration with UAV technology, as explored in studies by Shao et al. (2023) and, allows for a more localized and accurate estimation of crop water requirements. When combined with UAV-derived data, these models can significantly enhance the precision of irrigation scheduling, leading to more efficient water use and reduced waste.

Despite these advantages, the application of UAVs in irrigation management is challenging. One major limitation, as identified by Gao et al. (2021), is the need for advanced data processing capabilities to handle the large volumes of data generated by UAVs. Surface energy balance models, both single-source (e.g., METRIC, SEBAL, SSEBop) and two-source (e.g., TSEB, ALEXI, DTD) models, have been used for ET estimation (Taheri et al. 2022). Two-source models have generally shown higher accuracy in complex climatic conditions and varying vegetation levels (Li et al. 2021). TSEB, for instance, has been effectively applied in

various crops (Gao et al., 2023; Nassar et al., 2022; Sánchez et al., 2014; Song et al., 2016; Tunca et al., 2022).

Moreover, Nassar et al. (2022) highlight the challenges in integrating UAV data with traditional ET estimation models, which require calibration and validation for specific crops and regions. Additionally, the cost of UAV systems and their operational complexities, as discussed by Mohsan et al. (2022), can be prohibitive for small-scale farmers.

Looking towards the future, the potential of UAVs in irrigation management is vast. Feng et al. (2023) suggest that continued advancements in UAV technology and more sophisticated data analytics will enable even more precise and automated irrigation systems. This could lead to a paradigm shift in water resource management in agriculture, as Gao et al. (2023) envisioned, where UAVs play a central role in achieving sustainable and efficient use of water resources.

In conclusion, UAV systems present a significant opportunity to enhance irrigation management in agriculture. Integrating UAV-derived data with ET estimation models offers a path toward more precise and efficient water use. While challenges remain, particularly in data management and model integration, the future of UAVs in irrigation management is promising. As technology continues to evolve, it holds the potential to revolutionize how water resources are managed in agriculture, paving the way for more sustainable farming practices.

References

Cheng, M., Jiao, X., Liu, Y., Shao, M., Yu, X., Bai, Y., Wang, Z., Wang, S., Tuohuti, N., & Liu, S. (2022). Estimation of soil moisture content under high maize canopy coverage from UAV multimodal data and machine learning. *Agricultural Water Management, 264*, 107530,

Feng, J., Wang, W., Che, T., & Xu, F. (2023). Performance of the improved two-source energy balance model for estimating evapotranspiration over the heterogeneous surface. *Agricultural Water Management, 278*, 108159, https://doi.org/10.1016/j.agwat.2023.108159

Gao, R., Torres-Rua, A., Nassar, A., Alfieri, J., Aboutalebi, M., Hipps, L., Ortiz, N.B., Mcelrone, A.J., Coopmans, C., & Kustas, W. (2021). Evapotranspiration partitioning assessment using a machine-learning-based leaf area index and the two-source energy balance model with sUAV information. In, *Autonomous Air and Ground Sensing Systems*

for Agricultural Optimization and Phenotyping VI (p. 117470N): International Society for Optics and Photonics

Gao, R., Torres-Rua, A.F., Nieto, H., Zahn, E., Hipps, L., Kustas, W.P., Alsina, M.M., Bambach, N., Castro, S.J., & Prueger, J.H. (2023). ET Partitioning Assessment Using the TSEB Model and sUAS Information across California Central Valley Vineyards. *Remote Sensing, 15*, 756, https://doi.org/10.3390/rs15030756

Mohsan, S.A.H., Othman, N.Q.H., Khan, M.A., Amjad, H., & Żywiołek, J. (2022). A comprehensive review of micro UAV charging techniques. *Micromachines, 13*, 977,

Nassar, A., Torres-Rua, A., Hipps, L., Kustas, W., McKee, M., Stevens, D., Nieto, H., Keller, D., Gowing, I., & Coopmans, C. (2022). Using Remote Sensing to Estimate Scales of Spatial Heterogeneity to Analyze Evapotranspiration Modeling in a Natural Ecosystem. *Remote Sensing, 14*, 372,

Sánchez, J., López-Urrea, R., Rubio, E., González-Piqueras, J., & Caselles, V. (2014). Assessing crop coefficients of sunflower and canola using two-source energy balance and thermal radiometry. *Agricultural Water Management, 137*, 23-29,

Shao, G., Han, W., Zhang, H., Zhang, L., Wang, Y., & Zhang, Y. (2023). Prediction of maize crop coefficient from UAV multisensor remote sensing using machine learning methods. *Agricultural Water Management, 276*, 108064,

Song, L.S., Kustas, W.P., Liu, S.M., Colaizzi, P.D., Nieto, H., Xu, Z.W., Ma, Y.F., Li, M.S., Xu, T.R., Agam, N., Tolk, J.A., & Evett, S.R. (2016). Applications of a thermal-based two-source energy balance model using Priestley-Taylor approach for surface temperature partitioning under advective conditions. *Journal of Hydrology, 540*, 574-587,

Tunca, E. (2023). Evaluating the performance of the TSEB model for sorghum evapotranspiration estimation using time series UAV imagery. *Irrigation Science*, 1-18,

Tunca, E., Koksal, E.S., Torres-Rua, A., Kustas, W.P., & Nieto, H. (2022). Estimation of bell pepper evapotranspiration using two-source energy balance model based on high-resolution thermal and visible imagery from unmanned aerial vehicles. *Journal of Applied Remote Sensing, 16*https://doi.org/10.1117/1.JRS.16.022204

Zhang, Y., Han, W., Zhang, H., Niu, X., & Shao, G. (2023). Evaluating maize evapotranspiration using high-resolution UAV-based imagery and FAO-56 dual crop coefficient approach. *Agricultural Water Management, 275*, 108004,